



HAL
open science

Capturing dynamic ligand-to-metal charge transfer with a long-lived cationic intermediate for anionic redox

Biao Li, Khagesh Kumar, Indrani Roy, Anatolii Morozov, Olga Emelyanova, Leiting Zhang, Tuncay Koç, Stéphanie Belin, Jordi Cabana, Rémi Dedryvère, et al.

► To cite this version:

Biao Li, Khagesh Kumar, Indrani Roy, Anatolii Morozov, Olga Emelyanova, et al.. Capturing dynamic ligand-to-metal charge transfer with a long-lived cationic intermediate for anionic redox. *Nature Materials*, 2022, 21, pp.1165-1174. 10.1038/s41563-022-01278-2 . hal-03705453

HAL Id: hal-03705453

<https://univ-pau.hal.science/hal-03705453>

Submitted on 27 Mar 2024

HAL is a multi-disciplinary open access archive for the deposit and dissemination of scientific research documents, whether they are published or not. The documents may come from teaching and research institutions in France or abroad, or from public or private research centers.

L'archive ouverte pluridisciplinaire **HAL**, est destinée au dépôt et à la diffusion de documents scientifiques de niveau recherche, publiés ou non, émanant des établissements d'enseignement et de recherche français ou étrangers, des laboratoires publics ou privés.

9 **Capturing dynamic ligand-to-metal charge transfer with a long-lived cationic** 10 **intermediate for anionic redox**

11 Biao Li^{1,2}, Khagesh Kumar³, Indrani Roy³, Anatolii V. Morozov⁴, Olga V. Emelyanova⁴, Leiting Zhang⁵,
12 Tuncay Koç^{1,2,6}, Stéphanie Belin⁷, Jordi Cabana³, Rémi Dedryvère^{2,8}, Artem M. Abakumov⁴, Jean-Marie
13 Tarascon^{1,2,6*}

14 ¹Chimie du Solide-Energie, UMR 8260, Collège de France, 75231 Paris Cedex 05, France.

15 ²Réseau sur le Stockage Electrochimique de l'Energie (RS2E), FR CNRS 3459, France.

16 ³Department of Chemistry, University of Illinois at Chicago, Chicago, Illinois 60607, United States.

17 ⁴Center for Energy Science and Technology, Skolkovo Institute of Science and Technology, Nobel str. 3, 121205
18 Moscow, Russia.

19 ⁵Battery Electrodes and Cells, Electrochemistry Laboratory, Paul Scherrer Institute, Forschungsstrasse 111, 5232
20 Villigen-PSI, Switzerland. (Present address: Department of Chemistry – Ångström Laboratory, Uppsala University, Box 538,
21 SE-751 21 Uppsala, Sweden.)

22 ⁶Sorbonne Université, 4 Place Jussieu, 75005, Paris, France.

23 ⁷Synchrotron SOLEIL, L'orme des Merisiers, BP 48 Saint Aubin, 91192 Gif-sur-Yvette, France

24 ⁸IPREM, E2S-UPPA, CNRS, Univ. Pau & Pays Adour, Pau, France.

25 * Corresponding author: jean-marie.tarascon@college-de-france.fr

26

27 **Abstract**

28 Reversible anionic redox reactions represent a transformational change for creating advanced high-
29 energy-density positive electrode materials for Li-ion batteries. Their activation mechanism is
30 frequently linked to ligand-to-metal charge transfer (LMCT) processes, which have not been yet
31 fully validated experimentally due to the lack of suitable model materials. Here, we show that the
32 activation of anionic redox in cation-disordered rock-salt $\text{Li}_{1.17}\text{Ti}_{0.58}\text{Ni}_{0.25}\text{O}_2$ involves a long-lived
33 intermediate $\text{Ni}^{3+/4+}$ species, which can fully evolve to Ni^{2+} during relaxation. Combining
34 electrochemical analysis and spectroscopic techniques, we quantitatively identified that the
35 reduction of such $\text{Ni}^{3+/4+}$ goes through a dynamic LMCT process ($\text{Ni}^{3+/4+}\text{-O}^{2-} \rightarrow \text{Ni}^{2+}\text{-O}^{n-}$).
36 Besides providing the first experimental validation of previous theoretical hypothesis, our
37 finding also helps to rationalize several unusual peculiarities associated with anionic redox, such
38 as cationic-anionic redox inversion and voltage hysteresis. Altogether, this work provides
39 additional guidance for designing high-capacity electrodes by screening cationic species in
40 appropriately mediating ligand-to-metal charge transfer.

41
42
43

Main text

44 Li-ion batteries are the best performing for digitization of our society but their energy
45 density still needs a boost to overcome the “range anxiety” of electric vehicles. This calls for
46 positive electrodes (cathodes) hosting more Li ions per unit mass. The now-popular
47 transformational approach relies on Li-rich materials ($\text{Li}_{1+x}\text{M}_{1-x}\text{O}_2$, $0 < x < 1$, M denotes transition
48 metals), which deliver high capacities relying on both cationic and anionic redox processes¹⁻⁶.
49 Nevertheless, the extra capacity from anionic redox is associated with sluggish kinetics and voltage
50 hysteresis casting formidable challenges on practical implementation.^{4, 5, 7} Therefore, it calls for
51 further interrogating how the anionic redox is activated in order to understand and address these
52 issues.

53 To trigger anionic redox, thermodynamic band-structure considerations presume the need
54 of anion p lone-pair states pinned just below the Fermi level⁸⁻¹⁰. However, this scenario fails in
55 such cases like Li_2TiO_3 or Li_2TiS_3 , in which the anionic redox cannot be activated through anion
56 p-states lying at the top of the empty d-band of Ti^{4+} ^{11, 12}. Nevertheless, these electrochemically
57 inactive compounds can be activated by doping with either cations like $\text{Fe}^{2+}/\text{Fe}^{3+}$, Co^{2+} , and Ti^{3+} ,
58 or anions such as Se, both strategies enlist cationic redox simultaneously¹¹⁻¹⁵. Similar situation is
59 equally encountered in most of the d^0 -M based Li-rich oxides/sulfides², hence raising the universal
60 question of whether cationic redox is essential to activate anionic redox.

61 This essentiality was suggested nearly eight years ago, when anionic redox was envisaged
62 to go through a “reductive coupling” mechanism—that is an initial over-oxidation of M followed
63 by its reduction whilst anions are partially oxidized, such as $\text{Ru}^{6+}\text{-O}^{2-} \rightarrow \text{Ru}^{5+}\text{-O}^-$ in
64 $\text{Li}_2\text{Ru}_{0.75}\text{Sn}_{0.25}\text{O}_3$ ³. A similar two-step activation was proposed in $\text{Li}_2\text{Ir}_{0.75}\text{Sn}_{0.25}\text{O}_3$ ($\text{Ir}^{>5.5+}$ -

65 $O^{2-} \rightarrow Ir^{5.5+}-O^{(2-n)-}$), though named differently as “ligand-to-metal charge transfer (LMCT)”¹⁶.
66 This mechanism is also shared by the well-known $Li_{1.2}Ni_{0.13}Mn_{0.54}Co_{0.13}O_2$ (Li-rich NMC)
67 compound, for which a Mn^{7+} intermediate species was theoretically predicted and can be reduced
68 spontaneously via O-to-Mn charge transfer process¹⁷. Regardless the different nomenclature, all
69 these interpretations share a similar LMCT process that has never been directly observed, probably
70 because of short lifetime of these cationic intermediate species. Although a “ Fe^{4+} ” intermediate
71 was recently captured by Mössbauer spectroscopy in $Li_{1.17}Ti_{0.33}Fe_{0.5}O_2$ ¹⁸, the short-lived excited
72 $Fe^{4+}-O^{2-}$ state cannot be probed by diffraction and spectroscopic X-ray techniques, leaving LMCT
73 still a hypothesis.

74 Here, we show first direct experimental LMCT observation during the activation of anionic
75 redox in a cation-disordered $xLi_2TiO_3 \cdot (1-x)LiTi_{0.5}Ni_{0.5}O_2$ system. Concentrating on the
76 $0.4Li_2TiO_3 \cdot 0.6LiTi_{0.5}Ni_{0.5}O_2$ ($Li_{1.17}Ti_{0.58}Ni_{0.25}O_2$) member, we identified a redox mechanism
77 consisting of sequential $Ni^{2+} \rightarrow Ni^{3+/4+}$ and O oxidation on charge but surprisingly followed by a
78 sequential $Ni^{3+/4+} \rightarrow Ni^{2+}$ and O reduction on discharge. This $Ni^{3+/4+}$ is a kinetically-activated long-
79 lived intermediate rather than a thermodynamically stabilized species that we confirmed both
80 experimentally and theoretically. Combined with *in-situ* powder X-ray diffractions (XRD),
81 electrochemical analysis, hard X-ray photoemission spectroscopy (HAXPES) and scanning
82 transmission electron microscopy coupled with electron energy-loss spectroscopy (STEM-EELS),
83 we successfully captured the dynamic LMCT process whose reaction rate is highly temperature-
84 and time-dependent. We finally rationalized that this cationic intermediate is responsible for
85 several unusual peculiarities of the anionic redox electrodes, including cationic-anionic redox
86 inversion, voltage and structural hysteresis, and path dependence.

87 **Structure and electrochemistry.** $x\text{Li}_2\text{TiO}_3 \cdot (1-x)\text{LiTi}_{0.5}\text{Ni}_{0.5}\text{O}_2$ ($0 \leq x \leq 1$, denoted as $x\text{LTO}-$
88 $(1-x)\text{LTNO}$ hereafter) compounds were synthesized through a solid-state reaction from precursors
89 obtained via a sol-gel method (see Methods). The $\text{LiTi}_{0.5}\text{Ni}_{0.5}\text{O}_2$ end-member adopts a well-
90 crystallized cubic rock-salt structure, according to its XRD pattern (Fig.1a, bottom). On the
91 contrary, the Li_2TiO_3 end-member presents layered ordering evidenced by the (003) reflection,
92 with a honeycomb superstructure in the transition metal layer (Fig.1a, top). $x\text{Li}_2\text{TiO}_3 \cdot (1-$
93 $x)\text{LiTi}_{0.5}\text{Ni}_{0.5}\text{O}_2$ solid solutions preserve the cation-disordered structure of $\text{LiTi}_{0.5}\text{Ni}_{0.5}\text{O}_2$ (no 003
94 peak) until $x = 0.6$, at which the synthesis was stopped to keep the structure cation-disordered and
95 avoid complicating the study. A representative Rietveld refinement of the $x=0.4$ synchrotron XRD
96 (SXRD) pattern (Fig.1c) gives a perfect cubic rock-salt structure wherein all the cations randomly
97 sit in the $4a$ site (Fig.1d, lower inset), as further seen from the high-angle annular dark-field
98 scanning transmission electron microscopy (HAADF-STEM) image (Fig. 1d). However, [100]
99 electron diffraction (ED) pattern (Fig. 1d, upper inset) demonstrates a structured diffuse scattering
100 (white arrow indicated). This diffuse intensity is characteristic of a short-range cationic order with
101 octahedral $[\text{OLi}_3\text{M}_3]$ (or $[\text{OLi}_4\text{M}_2]$ due to Li excess) clusters¹⁹. Indeed, short fragments of the $\{111\}$
102 rock-salt planes consisting of dots of different brightness are clearly visible in the [110] HAADF-
103 STEM image (Supplementary Fig. 1a) indicating different population of atomic columns with the
104 Li and M cations.

105 The electrochemical response of every compound was checked versus Li/Li^+ in the 2.0-
106 4.8V potential range (Fig.1b). Both $\text{LiTi}_{0.5}\text{Ni}_{0.5}\text{O}_2$ and Li_2TiO_3 have limited electrochemical
107 activity due to their limited Li diffusion²⁰ and poor electronic conductivity, respectively. The solid
108 solutions $x\text{LTO}-(1-x)\text{LTNO}$ delivered decent capacities, which fades upon cycling as represented
109 by the $x=0.4$ member (Supplementary Fig. 2). Their electrochemical behavior involves two

110 plateaus that are dependent on the Ni content. As x decreases, the length of the high-voltage ($\sim 4\text{V}$)
111 plateau during discharge increases at the expense of the low-voltage ($\sim 2.2\text{V}$) plateau. Such two
112 plateaus with different kinetics, as uncovered by the GITT measurements (Supplementary Fig.3),
113 are reminiscent of Ni redox and O redox reported in similar compounds previously²¹.

114 **Redox mechanism.** To validate the redox mechanism, the representative 0.4LTO-
115 0.6LTNO compound was studied by both hard and soft *ex-situ* X-ray adsorption spectroscopy
116 (XAS) at states of charge (SoCs) marked in Fig.2a. Ti *K*- and Ti *L*_{2,3}-edge XAS (Supplementary
117 Fig.4) show that Ti⁴⁺ remains during the whole cycling process, with only subtle variations of the
118 local coordination environment inferred from changes in shape of the absorption edge and relative
119 intensity of the pre-edge features at the Ti *K*-edge²².

120 Unlike Ti, Ni does participate in the redox process, as clearly shown by the Ni *L*-edge
121 inverse partial-fluorescence-yield (iPFY) XAS²³ (Fig.2b) probing a ~ 100 nm depth and free of
122 self-absorption effects. The pristine sample (#1) has a Ni²⁺ initial state²⁴ that is further confirmed
123 by Ni *K*-edge XAS (Supplementary Fig.5b). The first-charge voltage slope (#1 \rightarrow #2, Fig.2a) is
124 apparently dominated by Ni²⁺ oxidation to Ni^{3+/4+} supported by the clear shift and growth of peaks
125 B and D²⁴ (Fig.2b). This is further verified by the O *K*-edge total-fluorescence-yield (TFY) XAS
126 on the same samples, where a pre-edge peak E at ~ 528 eV (#1 \rightarrow #2 in Fig.2c), corresponding to
127 an electronic transition from O 1s states to the empty O(2p)-Ni(3d) states²⁵, emerges upon
128 oxidation. The following charge process (#2 \rightarrow #3, Fig.2a) shows a slight Ni reduction rather than
129 oxidation according to the lowered intensity of peak B in Ni *L*-edge (Fig.2b), symbolizing an
130 oxygen redox mechanism that is normally associated with cationic reduction. This can be
131 ascertained by a sharp increase of pre-edge peak F in relative to peak G of the O *K*-edge XAS from
132 #2 \rightarrow #3 (Fig.2c), exclusively indicating the depopulation of O 2p electrons. Such oxygen redox

133 preceded by a cationic redox during charge is not surprising since the staircase curve observed in
134 Fig.2a is quite typical for Li-rich compounds. Moreover, the O₂ release during oxygen redox
135 process was checked with online electrochemical mass spectrometry (OEMS). Interestingly, at 1st
136 charge the oxygen release increases stepwise but with a total departure of only 1.2% O atom
137 (Supplementary Fig.6), indicative of the high reversibility of oxygen redox. Such stepwise oxygen
138 release caused by the various environments of O ions in cation-disordered structure
139 (Supplementary Fig.6) is also reproducible in the $x=0.2, 0.5$ members (Supplementary Fig. 7), but
140 it varies in amount: higher Ti content promotes more oxygen redox activity and O₂ evolution.

141 On discharge, Ni^{3+/4+} is largely reduced to a quasi-pristine state at the ~3.8 V
142 (pseudo)plateau (Fig. 2a, #3→#4), as evidenced by the peak B recovery in Ni *L*-edge iPFY XAS
143 (Fig.2b) and the nearly disappeared peak E in O *K*-edge XAS (Fig.2c). Upon further discharging
144 to the ~2.2V low-voltage plateau, peak F shrank to the equivalent height of peak G (#4→#5 in
145 Fig.2c) whereas Ni shows negligible contribution (peak B in Fig. 2b), indicating a sole O redox
146 mechanism. The redox process in the second charge generally mirrors the first: mainly Ni
147 oxidation followed by O oxidation (Supplementary Fig.8). Besides, the evolution of Ni valence
148 was further consistently confirmed by Ni *K*-edge XAS (Supplementary Fig.5).

149 Altogether, we recap the whole picture of the redox mechanism for 0.4LTO-0.6LTNO in
150 Fig. 2a with color-coded arrows. A Ni oxidation → O oxidation on charge follows by Ni reduction
151 → O reduction on discharge. This redox inversion behavior remains to be justified as it contradicts
152 usual expectations. It is also manifested by the voltage-window-opening experiment
153 (Supplementary Fig.9) that reveals a “path-dependent” feature alike Li-rich NMC materials²⁶.

154 To our surprise, the theoretical predictions of the redox mechanism for 0.4LTO-0.6LTNO
155 highly deviate from experimental results. DFT+*U* calculation predicted an energy-favorable

156 structure in which cations (Li/Ti/Ni) are distributed as homogeneously as possible (Supplementary
157 Fig.10a), consistent with the diffuse intensity observed from ED (Fig. 1d inset). However, 0.4LTO-
158 0.6LTNO shows sole O redox scenario upon Li removal as demonstrated by the calculated density
159 of states (DOS): the O 2p lone-pair states are depleted first as the Ni 3d occupied states are located
160 at a much lower energy (Fig. 2d and Supplementary Fig.10c-f). This should be attributed to the
161 large Mott-Hubbard U splitting of Ni 3d states, in a similar manner to isostructural NiO whose O
162 2p states are also higher in energy than Ni 3d states²⁷. The Bader charge analysis (Fig. 2e) further
163 confirms the charge transfer on O while Ni barely changes. We further explored what governs this
164 divergence between experimental and theoretical results.

165 **Structural evolution.** An *in situ* XRD analysis shows a solid-solution phase transition
166 behavior during the first two cycles (Fig.3a-3c) supported by lattice parameter evolution as a
167 function of time (Fig.3b) and Li content (Fig.3d). Unlike layered structures undergoing interlayer
168 repulsion upon delithiation, disordered rock-salt structure bypasses this cooperative effect due to
169 random cation occupation, hence its lattice variation is mainly sensitive to the M-O bond length.
170 On 1st charge the lattice shrinks linearly upon Ni oxidation due to the shortening of Ni-O bonds
171 (Fig.3b) with the slope decreases through the O oxidation region because O redox generally causes
172 local structural variation (O-O bond shortening, MO₆ distortion etc.) rather than collective M-O
173 bond length change²⁸. However, during discharge, Ni is reduced before O, hence we observe the
174 drastic expansion of the lattice due to the elongation of Ni-O bond, until triggering the O reduction
175 where the lattice parameter barely changes (Fig.3b). The second cycle almost mirrors the first
176 except for the steeper lattice parameter change during O redox. Therefore, in agreement with XAS
177 results, the lattice evolution also shows an inversion behavior from charge to discharge, causing
178 “structural hysteresis” (Fig. 3d), reminiscent of previous findings in Li-rich NMC²⁶. Moreover,

179 such “structural hysteresis” is also observed in other x LTO-(1- x)LTNO members (Supplementary
180 Fig. 11).

181 Rietveld refinements of SXR D patterns for samples in different cycling states
182 (Supplementary Fig.12 and Table 1) indicate that the cubic rock-salt structure of 0.4LTO-
183 0.6LTNO is well preserved. Only 1%~2% reversible cation migration (octahedral $4a \leftrightarrow$ tetrahedral
184 $8c$) was detected during the first cycle, further confirmed by HAADF-STEM images showing no
185 obvious cation migration to the tetrahedral sites (Fig.5e). Such negligible cation migration can
186 hardly be responsible for either the large voltage hysteresis or the pronounced redox inversion.
187 Notably, the lattice parameter of the fully charged sample (4.162 Å, Supplementary Fig.12b) is
188 surprisingly larger than the one (~4.111 Å) obtained from *in situ* XRD (Fig. 3d). Bearing in mind
189 that the sample (sealed in glass capillary) rested for around two months before SXR D data
190 acquisition, we collected SXR D pattern for another fully charged sample that only rested for two
191 weeks. The lattice parameter (4.141 Å, Supplementary Fig.13) was closer but still higher than that
192 for the charged state captured *in situ*. This observation was the first hint towards the metastable
193 nature of the charged sample, which can evolve with time until reaching a thermodynamically
194 stable state.

195 To verify our hypothesis, we directly charged the cell to 4.8 V and then opened the circuit
196 for relaxation (termed as in-electrolyte relaxation) while collecting *in situ* XRD patterns
197 (Supplementary Fig.14). A dramatic peak shift to lower angles was observed accompanied by a
198 drop in the open-circuit voltage (OCV). To exclude self-discharge (interactions between electrode
199 and electrolyte), we repeated *in situ* XRD experiment by relaxing an electrode out of electrolyte
200 once charged to 4.8V (Fig. 3e) and it generally replicates the in-electrolyte relaxation. For further
201 validation, an all-solid-state-battery (ASSB) was also assembled (see Methods), aiming to

202 eliminate the self-discharge (ASSB-relaxation, see Fig. 3f). The same peak shift was observed, as
203 guided by the arrows and color-coded bars in Fig.3f; 55°C heating was applied to accelerate the
204 relaxation (pink patterns) since the less oxidized state obtained by ASSB makes the relaxation
205 slower (Supplementary Fig.15). Since the lattice parameter is sensitive to the Ni oxidation state,
206 as previously mentioned, such peak shifting signifies lattice parameter increase due to Ni reduction
207 during relaxation. As no Ni redox was predicted by DFT calculations (Fig.2d,e), this implies that
208 $\text{Ni}^{3+}/\text{Ni}^{4+}$ could be an intermediate kinetically-stable species that could disappear via an internal
209 $\text{Ni}^{3+/4+} - \text{O}^{2-} \rightarrow \text{Ni}^{2+} - \text{O}^{\text{n-}}$ LMCT process.

210 **Capturing the LMCT process.** To inspect LMCT existence, we first rely on electrochemical
211 analysis. In our particular case the Ni and O reduction plateaus are highly decoupled (Fig. 2a), and
212 hence can be harnessed to directly gauge the Ni and O oxidation states based on the capacities (i.e.
213 electrochemical titration). By further discharging the electrode relaxed in the *in situ* XRD
214 experiment (Fig. 3e), it was found that the O reduction plateau (~2.2 V) increased by ~42 mA h g⁻¹
215 at the expense of Ni reduction plateau (~3.8 V), which almost totally vanished (Supplementary
216 Fig. 16). This rearrangement indicates a charge transfer from O to Ni during the relaxation process.

217 To validate LMCT more quantitatively, we relaxed the electrode by heating it under Ar at
218 various durations and temperatures (see electrochemical titration in Methods). The recovered
219 powders 1st charged to 4.5V were relaxed at temperatures from 25 °C to 140 °C for a fixed time
220 of 24h (Fig. 4a). At higher temperature, the discharge curves show shorter Ni reduction and longer
221 O reduction plateaus. The associated capacity rearrangement was statistically shown in the
222 histogram (Fig. 4a inset), for which at least three cells were tested for every temperature. Moreover,
223 the mass-normalized dQ/dV curves (Fig. 4b) behave consistently, with a decrease in the Ni
224 reduction peak and increase in O reduction upon increasing temperature. In turn, the same trend

225 was reproduced by fixing the heating temperature at 140 °C and varying the heating time from 0 s
226 to 24 h (Fig. 4c,d). The relaxation speed indeed exponentially decreases with the progressing
227 relaxation; it only took several minutes at the beginning of heating (0s → 90s) but 20 hours in the
228 end (4h → 24h) to obtain similar rearranged capacities (Fig. 4c). These results demonstrate that
229 Ni³⁺/Ni⁴⁺ species is indeed a long-lived intermediate, which gradually vanishes through LMCT
230 with the rate depending on the relaxation temperature and time. Note that such relaxation is not a
231 high-temperature-induced behavior, since relaxation also proceeds at room temperature but at a
232 much slower speed (Supplementary Fig.17).

233 The relaxation speed also depends on the SoC at which the powder was recovered, as
234 charging to higher voltage (4.8V) led to faster relaxation compared to lower voltage (~4.4 V, 200
235 mA h g⁻¹, Supplementary Fig.18). This relaxation can also be reproduced in the second cycle
236 (Supplementary Fig.19), confirming that Ni³⁺/Ni⁴⁺ is persistent intermediate species upon cycling.
237 Even after full relaxation, such Ni³⁺/Ni⁴⁺ intermediate can be re-activated in the second charge and
238 onward (Supplementary Fig.20), suggesting this relaxation is only an intra-cycle effect rather than
239 permanent change. However, during electrochemical titration (Fig.4a,c), the conversion of Ni
240 redox into O redox is not full because LMCT may also produce some electrochemically
241 irreversible Oⁿ⁻ species (e.g. O₂↑) (see discussions in Supplementary Fig. 16).

242 Such long-lived Ni³⁺/Ni⁴⁺ intermediates offer an unprecedented chance to directly capture
243 the LMCT process by spectroscopic techniques. In order to simultaneously acquire the electronic
244 information of both Ni and O, HAXPES measurement with a photon energy of 10 keV was
245 implemented on samples with different relaxation states. This photon energy makes the analysis
246 sufficiently sensitive to the lattice oxygen (probe depth ~40 nm) dramatically decreasing the
247 signals of surface oxygen species. Ti 2*p*, Ni 2*p* and O 1*s* HAXPES spectra were collected on the

248 recovered samples charged to 4.5 V and heated at 120 °C for different times (see Method). While
249 Ti^{4+} stays throughout the relaxation process (Supplementary Fig.21), the deconvolution of Ni 2p
250 spectra unequivocally shows the reduction of Ni as a function of heating time (Fig. 5a). In parallel,
251 oxygen is getting more oxidized (Fig. 5b), hence the clear evidence of LMCT. Such qualitative
252 trend of charge transfer from O to Ni is consistent with the electrochemical titrations, and is further
253 confirmed by Ni K-edge XAS results (Supplementary Fig. 23) and STEM-EELS measurements
254 (Supplementary Fig. 24). Moreover, HAXPES data for the samples charged to 200 mA h g⁻¹ (~4.4
255 V) show similar results (Supplementary Fig. 25), further validating LMCT.

256 The LMCT was accompanied by a certain structural relaxation in addition to bond length
257 change. HAADF-STEM images and ED patterns from charged and relaxed samples (Fig.5e-5f)
258 show that the cubic rock-salt structure retains without noticeable cation migration to the tetrahedral
259 sites. However, diffuse intensity in the ED patterns vanished in the charged sample (Fig.5e inset)
260 but recurred back in the relaxed sample (Fig.5f inset), albeit being located at different positions
261 compared with the pristine one (Fig.1d inset). As the cationic columns barely change upon
262 relaxation (Supplementary Fig.1d-1c), this new diffuse intensity suggests a variation of Li⁺ and
263 cation vacancy ordering that is most probably driven by Ni-O charge redistribution for maintaining
264 local charge neutrality.

265 **Rationalizing redox inversion and voltage hysteresis.** Combining all results, it is clear that
266 $\text{Ni}^{3+/4+}$ is an intermediate species that will vanish via a LMCT process, rather than a
267 thermodynamically favored redox species. The activation of such $\text{Ni}^{3+/4+}$ excited states is
268 reminiscent of our previous findings in $\text{Li}_{1.17}\text{Ti}_{0.33}\text{Fe}_{0.5}\text{O}_2$, in which a Fe^{4+} intermediate species is
269 kinetically activated to trigger the oxygen redox activity¹⁸. Similarly, the appearance of $\text{Ni}^{3+/4+}$ can
270 also be rationalized through Marcus theory.^{18, 29} The electron removal from O 2p lone-pair states

271 involving large structural distortion is difficult (non-adiabatic process) whereas the electron
272 removal from σ -type Ni 3d-O2p delocalized states is more kinetically favorable (adiabatic process).
273 Therefore, charging the electrode will first create an excited kinetically stable Ni^{3+/4+} state that
274 lowers the local structural symmetry through a Jahn-Teller distortion and increases the Ni-O orbital
275 hybridization, which facilitates an internal charge transfer from O 2p lone-pair states to Ni^{3+/4+},
276 resulting in a Ni²⁺ – Oⁿ⁻ ground state. Note that here the “Ni^{3+/4+}” species could be more precisely
277 interpreted as “Ni 3d<sup>8- δ L” (*L* denotes holes in O 2p states hybridized with Ni 3d), since Ni³⁺-O²⁻
278 and Ni⁴⁺-O²⁻ were frequently associated with electron holes in O 2p band^{30,31}.</sup>

279 Unlike previous cases, the unicity of this Ni^{3+/4+} intermediate species is rooted in its long
280 lifetime, hence a large amount of Ni^{3+/4+} residue is preserved at the end of charge. Once subjected
281 to discharge, such preserved Ni^{3+/4+} species will be first reduced electrochemically due to its high
282 instability (Fig. 6a) as well as its higher electron transfer kinetics than O redox, as informed by
283 quantitative electrochemical analysis (Supplementary note I). This causes the unusual cationic-
284 anionic redox inversion behavior with asymmetry between charge and discharge (Fig.6a,b), which
285 also induces a structural hysteresis, as Ni intermediate redox dictates the evolution of bond length
286 and lattice parameter. Finally, a path-dependent feature can be observed, as opening the charging
287 voltage window will shift the SoCs during intermediate redox (Supplementary Fig. 26).

288 Our finding can also for the first time establish a quantitative picture for explaining voltage
289 hysteresis. We tried to determine the equilibrium potential through GITT, but the voltage gap
290 between charge and discharge never closed even under high temperature (55 °C) or long-period
291 relaxations (Supplementary Fig. 27) due to long-lived Ni intermediates. An efficient full relaxation
292 is essential to eliminate Ni intermediates in order to reach an equilibrium state (potential). To avoid
293 self-discharge disturbance, we mimicked the relaxation by heating the recovered powders (1C

294 4.5V), and then placed them back into fresh electrochemical cells. The OCV of these fresh cells
295 decreases as a function of heating time (yellow arrow in Fig. 6e). This trend is clearer as observed
296 from the very stable OCV during 15 min resting period (inset in Fig. 6e). Moreover, by plotting
297 the OCVs of the relaxed samples versus the fraction of remaining Ni intermediates determined
298 from the Ni redox capacity (Fig. 6f), one can find a solid linear positive relationship between them.
299 By extrapolating the least-square fitted line to 0% Ni intermediates, we obtained 3.74(2) V as an
300 estimate of the equilibrium potential when the Ni intermediates are absent. Such equilibrium
301 potential lies at exactly the gap between the GITT equilibriums of charge and discharge
302 (Supplementary Fig. 27c), and is in good consistency with experimentally determined one by
303 nearly fully relaxing the electrode (Supplementary Fig. 28). This way, we can deduce that the
304 charge overpotential, namely, the difference between OCV and equilibrium potential (green
305 double-headed arrow in Fig. 6f), increases linearly as a function of the amount of Ni intermediates.
306 Our analysis hence quantitatively validates the role of cationic intermediates in voltage hysteresis
307 for anionic-redox compounds, as more thoroughly discussed in Supplementary note II.

308 **Discussion.** Overall, we successfully captured the LMCT process during the activation of anionic
309 redox in Li-Ti-Ni-O compounds enabled by the unique long-lived Ni^{3+/4+} intermediate. It also
310 helped us to rationalize several unusual behaviors across different anionic redox compounds, as
311 discussed below. First, LMCT process is probably essential to trigger the anionic redox activity
312 from anion *p* lone-pair states. The core of triggering LMCT is that electron removal from O 2*p*
313 lone-pair states is kinetically difficult since it requires large structural distortion (e.g. O-O
314 dimerization). Instead, electrons will be more favorably removed from M *d* states first to form an
315 excited state, which then de-excites to ground state by taking electrons from ligands (i.e. LMCT).
316 Supporting examples are rich. Most of the pure *d*⁰/*d*¹⁰-M based Li-rich oxides or sulfides/selenides

317 (e.g. Li_2TiO_3 , Li_3NbO_4 , Li_4MoO_5 , Li_2TiS_3 , Li_2TiSe_3 etc.)^{2, 11-15} are electrochemically inactive
318 simply due to the kinetic limitation of electron removal from ligand p lone-pair states. However,
319 anionic redox is active in all the d^n -M ($n>0$) based Li-rich oxides (M=Mn, Ni, Ru, Ir)³²⁻³⁴ or their
320 derivatives^{3,16,35}, and also in d^0/d^{10} -M based Li-rich oxides/sulfides doped with
321 $\text{Ni}^{2+}/\text{Fe}^{2+}/\text{Fe}^{3+}/\text{Co}^{2+}/\text{Mn}^{3+}/\text{Ti}^{3+}$ ^{2,11-15,18,21,36-38}, because they have d electrons that can be removed
322 to form cationic excited states. Besides, anionic redox can be activated by anion substitution
323 ($\text{Li}_2\text{TiS}_y\text{Se}_{3-y}$)¹⁴ or moving from Li to Na (Na_2TiS_3)³⁹, where evidences of Ti^{3+} species were found
324 capable of providing additional d electrons. These numerous cases imply the crucial role of M ions
325 with removable d electrons in triggering anionic redox, but it was not clear what role are these M
326 ions playing until LMCT in this work comes as a final piece of the puzzle. The essentiality of
327 LMCT to activate anionic redox was further validated by our experiment that $\text{Ni}^{3+/4+}$ will always
328 be re-triggered even at a ground state in O redox region ([Supplementary Figure S29](#)).

329 Besides, we believe the long-lived $\text{Ni}^{3+/4+}$ intermediates are also present in most of the Ni-
330 containing d^0 -M based Li-rich compounds (e.g. $\text{Li}_{1.3}\text{Ni}_{0.27}\text{Ta}_{0.43}\text{O}_2$, $\text{Li}_{1.3}\text{Ni}_{0.27}\text{Nb}_{0.43}\text{O}_2$, and
331 $\text{Li}_{4.15}\text{Ni}_{0.85}\text{WO}_6$)^{15,21,37,38}, as they share very similar structures and electrochemical profiles with
332 Li-Ni-Ti-O compounds. Redox inversion and voltage hysteresis were also observed in these
333 compounds, although a band-inversion theory was proposed earlier to explain them^{10,21}. Band-
334 inversion gives good thermodynamic considerations but falls in short of rationalizing the kinetic
335 effect, as detailed in [Supplementary note III](#). By contrast, LMCT provides a more comprehensive
336 picture in accounting for both thermodynamics and kinetics, corroborated by compelling evidences.
337 More importantly, a very similar cationic-anionic redox inversion can be found in the well-known
338 Li-rich NMC material ([Fig.6c,d](#)). Recalling previous findings frequently showing a Ni oxidation
339 followed by its reduction during charge process in these systems³⁵, it is possible that similar Ni

340 intermediates also exist in Li-rich NMC compounds alike Li-Ti-Ni-O systems, both suffering from
341 redox inversion, voltage/structural hysteresis, and path dependence. This can be partially
342 confirmed by the relaxation experiments on layered $\text{Li}_{1.2}\text{Ni}_{0.13}\text{Mn}_{0.54}\text{Co}_{0.13}\text{O}_2$ and $\text{Li}_{1.2}\text{Ni}_{0.2}\text{Mn}_{0.6}\text{O}_2$
343 compounds (Supplementary Fig.30-Fig.31). Specially, similar capacity rearrangement behavior
344 between layered $\text{Li}_{1.2}\text{Ni}_{0.2}\text{Mn}_{0.6}\text{O}_2$ and disordered $\text{Li}_{1.17}\text{Ni}_{0.25}\text{Ti}_{0.58}\text{O}_2$ (Supplementary Fig. 31)
345 indicates that LMCT could be a universal behavior for Li-rich materials regardless of the cation
346 ordering.

347 A further question regards why $\text{Ni}^{3+/4+}$ intermediate is more long-lived than others (e.g.
348 Ru^{6+} , Mn^{7+} , Fe^{4+}). Indeed, the lifetime of the cationic intermediates highly relies on the M-O bond
349 covalence. This can be inferred from the decreasing LMCT rate in Li-Ti-Ni-O compounds with
350 the reaction progressing due to the weakening covalence between Ni and O (Fig.4c). This is also
351 theoretically true as higher covalence means higher orbital hybridization and electronic coupling,
352 and hence lower energy barrier for electron transfer.⁴⁰ Such dependence is conducive for
353 understanding the electrochemical behaviors in different compounds. The lifetime of the cationic
354 intermediates decreases in the order of $\text{Ni}^{3+/4+} > \text{Fe}^{4+} > \text{Ru}^{6+}$ due to increasing M-O covalence
355 (Supplementary Fig.32). Long-lived intermediates like $\text{Ni}^{3+/4+}$ will induce a cationic-anionic redox
356 inversion with large chemical and electrochemical asymmetry between charge and discharge. This
357 unusual behavior is less remarkable for a compound having medium-lifetime intermediate, such
358 as $\text{Li}_{1.17}\text{Ti}_{0.33}\text{Fe}_{0.5}\text{O}_2$ (Fe^{4+} , Supplementary Fig. 32b)¹⁸, and totally absent for $\text{Li}_2\text{Ru}_{0.75}\text{Sn}_{0.25}\text{O}_3$ with
359 transient Ru^{6+} intermediate (Supplementary Fig. 32c)³.

360 Finally, our study also provides a guide to further high-capacity cathode design based on
361 anionic redox by screening appropriate cationic intermediate. This can be done by choosing a high-
362 covalent M-O system to speed up the oxygen redox kinetics, or by fully retarding anionic redox

363 with a very long-lived cationic intermediates so as to utilize more cationic redox. A delicate
364 balance between these two extremities may help us to smartly utilize cationic and anionic redox in
365 Li-rich compounds thus achieving high energy density but avoiding practical limitations. Besides,
366 LMCT is common in the field of luminescence, photosensitization, and photocatalysis.⁴¹⁻⁴² While
367 long-lived LMCT states have been long pursued in high-performance photosensitizers and
368 photoelectrocatalysis, our finding of such long-lived intermediates by electrochemical methods
369 shows their potential applicability in related fields and beyond. In a broader sense, our
370 experimental validation of LMCT, as the first report of this phenomenon in solids with periodic
371 crystal structure, provides great opportunities for chemists and physicists to investigate electron
372 transfer phenomenon in similar mediums.

373

374

375 **Acknowledgements**

376 This research used resources of the Advanced Photon Source, a US Department of Energy (DOE) Office
377 of Science User Facility, operated for the DOE Office of Science by Argonne National Laboratory under
378 Contract No. DE-AC02-06CH11357. We are grateful to John Freeland, Tianpin Wu and George Sterbinsky
379 for their help during mail-in XAS measurements at the Advanced Photon Source. J.C. and I.R. acknowledge
380 support from the National Science Foundation, under Grant No. DMR-1809372. K.K. acknowledges
381 support from the National Science Foundation, under Grant No. CBET-1800357. A.A. and A.M. are
382 grateful to the Russian Science Foundation for financial support (grant 20-13-00233). Access to TEM
383 facilities was granted by the Advance Imaging Core Facility of Skoltech. HAXPES experiments (proposal
384 #99210184) were performed on the GALAXIES beamline at SOLEIL Synchrotron, France. The Ni K-edge
385 XAS was collected on ROCK beamline at SOLEIL Synchrotron through a rapid access for urgent need.
386 We are grateful to Jonas Sottmann and Jean-Pascal Rueff for their assistance during the HAXPES
387 experiments. J.-M.T and B.L. acknowledge funding from the European Research Council (ERC)
388 (FP/2014)/ERC Grant-Project 670116-ARPEMA.

389

390 **Additional information**

391 Supplementary information is available for this paper at xxxx.
392 Correspondence and requests for materials should be addressed to J.M.T.

393

394

395 **Author contributions**

396 B.L. and J.-M.T. conceived the idea and designed the experiments. B.L. carried out the synthesis, structural
397 characterization, electrochemical analysis and DFT calculations. R.D. collected and analyzed the HAXPES
398 data. K.K., I.R., and J.C. collected the XAS data and carried out the analysis. A.M., O.E, and A.A.
399 performed TEM experiments and did the analysis. L.Z. did the OEMS experiments and data analysis. S.B.
400 collected the Ni K-edge XAS data during relaxation. T.K. did the protocol and assembling of ASSB cells.
401 B.L. and J.-M.T. wrote the manuscript with the contributions from all the authors.

402

403 **Competing interests**

404 The authors declare no competing interests.

405

406

407 **Figure captions**

408 **Figure 1. Structure and electrochemistry of $x\text{Li}_2\text{TiO}_3\cdot(1-x)\text{LiTi}_{0.5}\text{Ni}_{0.5}\text{O}_2$ ($0 < x < 1$).** **a**, XRD patterns. **b**,
409 Galvanostatic charge and discharge curves (first 2 cycles) at a current density of 20 mA g^{-1} in the voltage
410 range of 2.0-4.8V. For Li_2TiO_3 , a low current density of 5 mA g^{-1} was used. **c**, Rietveld refinement results
411 for the SXRD of $x=0.4$ member (0.4LTO-0.6LTNO, or $\text{Li}_{1.17}\text{Ti}_{0.58}\text{Ni}_{0.25}\text{O}_2$). **d**, [001] HAADF-STEM image
412 of the pristine 0.4LTO-0.6LTNO sample, with the corresponding [001] ED pattern and crystal structure
413 shown as insets. The white arrow in the ED pattern indicates the diffuse intensity originated from short-
414 range ordering.

415 **Figure 2. Redox mechanism of 0.4LTO-0.6LTNO compound studied by *ex situ* XAS and DFT**
416 **calculations.** **a**, cycling curve of 0.4LTO-0.6LTNO compound with specific points marked out for *ex situ*
417 XAS studies. The points were numbered sequentially corresponding to the spectra shown in **b** and **c**. The
418 annotated colored arrows highlight the redox processes inferred from the XAS results. **b**, Ni *L*-edge IPFY-
419 XAS results. The spectra have two different regions corresponding to L_3 and L_2 edges, respectively, due to
420 the spin-orbit splitting, with each further split into two peaks (electron transition of Ni $2p \rightarrow$ Ni $3d-t_{2g}$ and
421 $3d-e_g$, respectively) caused by octahedral ligand field effect. **c**, O *K*-edge TFY-XAS results. The pre-edge
422 peaks (525-536 eV) corresponds to the electron transition from O ($1s$) to unoccupied O($2p$)-Ni/Ti ($3d$)
423 hybridized states. **d**, Calculated DOS of 0.4LTO-0.6LTNO compound during lithium removal within a
424 DFT+*U* framework. Fermi level is marked by a vertical dashed line. **e**, The charge transfer for both Ni and
425 O during delithiation process of 0.4LTO-0.6LTNO identified by calculated Bader charge.

426 **Figure 3. *In situ* XRD patterns for 0.4LTO-0.6LTNO.** **a**, first two electrochemical cycles between 4.8
427 and 2 V. **b**, evolution of the *a* lattice parameter (with error bar indicating standard deviation) extracted from
428 *in situ* XRD patterns. **c**, *in situ* XRD patterns for the first two cycles. The Ni and O oxidation/reduction
429 processes are highlighted by color-coded bands and texts. **d**, lattice parameter change as a function of Li
430 content. The Ni redox and O redox regions are highlighted with green and pink shades, respectively. A
431 large hysteresis is highlighted between the lattice parameter change on charge and discharge. **e**, *In situ* XRD
432 collected on an electrode rapidly recovered from a liquid cell charged to 4.8V, followed by washing and
433 drying (out-of-electrolyte relaxation). **f**, *In situ* XRD on an electrode recovered from an ASSB in order to
434 eliminate self-discharge due to liquid electrolyte. The dark to green patterns were collected with continuous

435 XRD scans while shaded pink patterns were collected after 55°C treatment for different time. A clear peak
436 shift is indicated by the colored bars at the top directed by a black arrow.

437 **Figure 4. Quantifying the LMCT process by electrochemical titration.** **a**, discharge curves for samples
438 that were relaxed at different temperatures for 24h. The samples were recovered from one batch of powder
439 charged to 4.5 V and then divided into several equal portions for heating. The discharge curve of a dried
440 sample without heating was attached together for benchmarking. The capacities of Ni redox plateau (4.5-
441 2.5 V) and O redox plateau (2.5-1.85 V) were extracted from the discharge curve and plotted as histogram
442 as inset. At least three cells were assembled for every sample in order to statistically quantify the charge
443 transfer (as shown by the error bars indicating the standard deviation in the histogram). Correspondingly,
444 the dQ/dV curves in **b** show the capacity rearrangement between Ni and O redox. Note the O reduction
445 peaks were slightly aligned to the same position in order to easily observe the peak intensity change. **c,d**,
446 discharge curves and their corresponding dQ/dV curves of samples that were relaxed at 140 °C for different
447 times. The sample preparation and cell assembly were done in the same manner as in **a**.

448 **Figure 5. LMCT characterized by HAXPES with an $h\nu=10$ keV photon energy and structural**
449 **analysis.** **a,b**, Ni 2p spectra and O 1s spectra of the samples charged to 4.5V and relaxed under heating at
450 120 °C for different time, as guided by the arrow in the left. The ratio of Ni²⁺ and Oⁿ⁻ species is indicated
451 beside the corresponding peaks. **c**, Ni 2p spectrum of pristine 0.4LTO-0.6LTNO reference sample showing
452 a pure Ni²⁺ signal. **d**, O 1s spectrum of Li-rich NMC reference sample charged to 4.8V³⁵. More reference
453 data are shown in Supplementary Fig. 22. Ni 2p spectra were fitted as a linear combination of two reference
454 curves: Ni²⁺ from pristine 0.4LTO-0.6LTNO and Ni^{3+/4+} from fully charged Li-rich NMC
455 (Supplementary Fig. 22b). The deconvolution of O 1s spectra gave three difference species: (1) lattice O²⁻
456 at ~529.5 eV (gradient grey); (2) oxidized lattice oxygen species Oⁿ⁻ (0<n<2) at ~530.5 eV (gradient red);
457 (3) the surface oxygenated species like carbonates etc. (unfilled curves). “Sat.” denotes satellite peaks
458 associated to Ni 2p peaks (in **a**) and lattice O²⁻ peak (in **b**). **e,f**, [001] HAADF-STEM images of 0.4LTO-
459 0.6LTNO charged to 4.5 V before and after relaxation (at 140 °C for 24h) with corresponding [001] ED
460 patterns.

461 **Figure 6. Rationalizing redox inversion and voltage hysteresis.** **a**, 2nd cycle of the 0.4LTO-0.6LTNO
462 compound with different cutoff voltage, with the corresponding dQ/dV profiles shown in **b**. A Ni-O redox
463 inversion is highlighted by a coupled arrow pair. **c,d**, 2nd cycle of Li-rich NMC compound with different
464 cutoff voltages and their corresponding dQ/dV curves. In the same way with 0.4LTO-0.6LTNO compound,
465 a cationic-anionic redox inversion behavior is highlighted. **e**, Discharge curves of samples relaxed to
466 different states. The samples were recovered from a same batch powder charged to 4.5 V and then heated
467 at 120 °C for different time (from 0 s to 24 h, as indicated by the black horizontal arrow). An in-cycling
468 discharge curve after charging to 4.5 V was incorporated together for comparison. Inset shows the OCV
469 evolution as a function of resting time before involved into discharge. Orange arrow indicates the less the
470 Ni intermediate (inferred from the Ni reduction plateau), the lower the OCV. **f**, Fitting of the OCV vs.
471 fraction of Ni intermediates dataset by least square method. The fractions of Ni intermediates were obtained
472 via dividing the Ni reduction capacity of every relaxed sample by the full Ni reduction capacity of in-
473 cycling sample (set as 100%).

474

475

476

477

478 **References**

- 479 1. Rozier, P. & Tarascon, J.M. “Review—Li-Rich Layered Oxide Cathodes for Next-Generation Li-
480 Ion Batteries: Chances and Challenges”. *J. Electrochem. Soc.* **162**, A2490 (2015).
- 481 2. Yabuuchi, N. Material Design Concept of Lithium-Excess Electrode Materials with Rocksalt-
482 Related Structures for Rechargeable Non-Aqueous Batteries. *Chem. Rec.* **19**, 690 (2018).
- 483 3. Sathiya, M. et al. Reversible anionic redox chemistry in high-capacity layered-oxide electrodes.
484 *Nat. Mater.* **12**, 827-835 (2013).
- 485 4. Assat, G. & Tarascon, J.-M. Fundamental understanding and practical challenges of anionic redox
486 activity in Li-ion batteries. *Nat. Energy* **3**, 373-386 (2018).
- 487 5. Li, B. & Xia, D. Anionic Redox in Rechargeable Lithium Batteries. *Adv. Mater.* **29**, 1701054
488 (2017).
- 489 6. Li, M. et al. Cationic and anionic redox in lithium-ion based batteries. *Chem. Soc. Rev.* **49**, 1688-
490 1705 (2020).
- 491 7. Assat, G., Delacourt, C., Corte, D.A.D. & Tarascon, J.-M. Editors' Choice—Practical Assessment
492 of Anionic Redox in Li-Rich Layered Oxide Cathodes: A Mixed Blessing for High Energy Li-Ion
493 Batteries. *J. Electrochem. Soc.* **163**, A2965-A2976 (2016).
- 494 8. Seo, D.H. et al. The structural and chemical origin of the oxygen redox activity in layered and
495 cation-disordered Li-excess cathode materials. *Nat. Chem.* **8**, 692-697 (2016).
- 496 9. Abakumov, A.M., Fedotov, S.S., Antipov, E.V. & Tarascon, J.M. Solid state chemistry for
497 developing better metal-ion batteries. *Nat. Commun.* **11**, 4976 (2020).
- 498 10. Ben Yahia, M., Vergnet, J., Saubanere, M. & Doublet, M.L. Unified picture of anionic redox in
499 Li/Na-ion batteries. *Nat. Mater.* **18**, 496–502 (2019).
- 500 11. Li, B. et al. Thermodynamic Activation of Charge Transfer in Anionic Redox Process for Li-Ion
501 Batteries. *Adv. Funct. Mater.* **28**, 1704864 (2018).
- 502 12. Saha, S. et al. Exploring the bottlenecks of anionic redox in Li-rich layered sulfides. *Nat. Energy*
503 **4**, 977-987 (2019).
- 504 13. Flamary-Mespoulie, F. et al. Lithium-rich layered titanium sulfides: Cobalt- and Nickel-free high
505 capacity cathode materials for lithium-ion batteries. *Energy Stor. Mater.* **26**, 213-222 (2020).
- 506 14. Leube, B.T. et al. Activation of anionic redox in d(0) transition metal chalcogenides by anion
507 doping. *Nat. Commun.* **12**, 5485 (2021).
- 508 15. Yabuuchi, N. et al. High-capacity electrode materials for rechargeable lithium batteries: Li₃NbO₄-
509 based system with cation-disordered rocksalt structure. *Proc. Natl. Acad. Sci. U S A* **112**, 7650-
510 7655 (2015).
- 511 16. Hong, J. et al. Metal-oxygen decoordination stabilizes anion redox in Li-rich oxides. *Nat. Mater.*
512 **18**, 256-265 (2019).
- 513 17. Radin, M.D., Vinckeviciute, J., Seshadri, R. & Vander Ven, A. Manganese oxidation as the origin
514 of the anomalous capacity of Mn-containing Li-excess cathode materials. *Nat. Energy* **4**, 639-646
515 (2019).
- 516 18. Li, B. et al. Correlating ligand-to-metal charge transfer with voltage hysteresis in a Li-rich rock-
517 salt compound exhibiting anionic redox. *Nat. Chem.* **13**, 1070-1080 (2021).
- 518 19. De Ridder, R., van Tendeloo, G. & Amelinckx, S. A cluster model for the transition from the short-
519 range order to the long-range order state in f.c.c. based binary systems and its study by means of
520 electron diffraction. *Acta Crystallogr. A* **32**, 216-224 (1976).
- 521 20. Lee, J. et al. Unlocking the potential of cation-disordered oxides for rechargeable lithium batteries.
522 *Science* **343**, 519-522 (2014).
- 523 21. Jacquet, Q. et al. Charge Transfer Band Gap as an Indicator of Hysteresis in Li-Disordered Rock
524 Salt Cathodes for Li-Ion Batteries. *J. Am. Chem. Soc.* **141**, 11452-11464 (2019).
- 525 22. Farges, F. Coordination of Ti⁴⁺ in silicate glasses: A high-resolution XANES spectroscopy study
526 at the Ti Kedge. *Am. Mineral.* **82**, 36-43 (1997).

- 527 23. Achkar, A.J., Regier, T.Z., Monkman, E.J., Shen, K.M. & Hawthorn, D.G. Determination of total
528 x-ray absorption coefficient using non-resonant x-ray emission. *Sci. Rep.* **1**, 182 (2011).
- 529 24. Qiao, R. et al. Direct Experimental Probe of the Ni(II)/Ni(III)/Ni(IV) Redox Evolution in
530 $\text{LiNi}_{0.5}\text{Mn}_{1.5}\text{O}_4$ Electrodes. *J. Phys. Chem. C* **119**, 27228-27233 (2015).
- 531 25. Yoon, W.-S., Chung, K.Y., McBreen, J., Fischer, D.A. & Yang, X.-Q. Changes in electronic
532 structure of the electrochemically Li-ion deintercalated LiNiO_2 system investigated by soft X-ray
533 absorption spectroscopy. *J. Power Sources* **163**, 234-237 (2006).
- 534 26. Croy, J.R. et al. Examining Hysteresis in Composite $x\text{Li}_2\text{MnO}_3 \cdot (1-x)\text{LiMO}_2$ Cathode Structures.
535 *J. Phys. Chem. C* **117**, 6525-6536 (2013).
- 536 27. Sawatzky, G.A. & Allen, J.W. Magnitude and Origin of the Band Gap in NiO. *Phys. Rev. Lett.* **53**,
537 2339-2342 (1984).
- 538 28. Assat, G., Iadecola, A., Delacourt, C., Dedryvère, R. & Tarascon, J.-M. Decoupling Cationic–
539 Anionic Redox Processes in a Model Li-Rich Cathode via Operando X-ray Absorption
540 Spectroscopy. *Chem. Mater.* **29**, 9714-9724 (2017).
- 541 29. Marcus, R.A. Electron transfer reactions in chemistry. Theory and experiment. *Rev. of Mod. Phys.*
542 **65**, 599-610 (1993).
- 543 30. Kim, M.G. et al. Ni and oxygen K-edge XAS investigation into the chemical bonding for lithiation
544 of $\text{Li}_y\text{Ni}_{1-x}\text{Al}_x\text{O}_2$ cathode material. *Electrochim. Acta* **50**, 501-504 (2004).
- 545 31. Kleiner, K. et al. On the Origin of Reversible and Irreversible Reactions in $\text{LiNi}_x\text{Co}_{(1-x)/2}\text{Mn}_{(1-x)/2}\text{O}_2$.
546 *J. Electrochem. Soc.* (2021). Doi: 10.1149/1945-7111/ac3c21.
- 547 32. Zhuo, Z. et al. Distinct Oxygen Redox Activities in Li_2MO_3 (M = Mn, Ru, Ir). *ACS Energy Letters*
548 **6**, 3417-3424 (2021).
- 549 33. Bianchini, M. et al. From LiNiO_2 to Li_2NiO_3 : Synthesis, Structures and Electrochemical
550 Mechanisms in Li-Rich Nickel Oxides. *Chemistry of Materials* **32**, 9211-9227 (2020).
- 551 34. Pearce, P.E. et al. Evidence for anionic redox activity in a tridimensional-ordered Li-rich positive
552 electrode $\beta\text{-Li}_2\text{IrO}_3$. *Nat. Mater.* **16**, 580-586 (2017).
- 553 35. Assat, G. et al. Fundamental interplay between anionic/cationic redox governing the kinetics and
554 thermodynamics of lithium-rich cathodes. *Nat. Commun.* **8**, 2219 (2017).
- 555 36. Yabuuchi, N. et al. Origin of stabilization and destabilization in solid-state redox reaction of oxide
556 ions for lithium-ion batteries. *Nat. Commun.* **7**, 13814 (2016).
- 557 37. Taylor, Z.N. et al. Stabilization of O-O Bonds by d(0) Cations in $\text{Li}_{4+x}\text{Ni}_{1-x}\text{WO}_6$ ($0 \leq x \leq 0.25$)
558 Rock Salt Oxides as the Origin of Large Voltage Hysteresis. *J. Am. Chem. Soc.* **141**, 7333-7346
559 (2019).
- 560 38. Yabuuchi, N., Tahara, Y., Komaba, S., Kitada, S. & Kajiyama, Y. Synthesis and Electrochemical
561 Properties of $\text{Li}_4\text{MoO}_5\text{-NiO}$ Binary System as Positive Electrode Materials for Rechargeable
562 Lithium Batteries. *Chem. Mater.* **28**, 416-419 (2016).
- 563 39. Leube, B.T. et al. Layered Sodium Titanium Trichalcogenide Na_2TiCh_3 Framework (Ch = S, Se):
564 A Rich Crystal and Electrochemical Chemistry. *Chem. Mater.* (2022) doi:
565 10.1021/acs.chemmater.1c04374.
- 566 40. Barbara, P.F., Meyer, T.J. & Ratner, M.A. Contemporary Issues in Electron Transfer Research. *J.*
567 *Phys. Chem. C* **100**, 13148-13168 (1996).
- 568 41. Wegeberg, C. & Wenger, O.S. Luminescent First-Row Transition Metal Complexes. *JACS Au* **1**,
569 1860-1876 (2021).
- 570 42. Chabera, P. et al. A low-spin Fe(III) complex with 100-ps ligand-to-metal charge transfer
571 photoluminescence. *Nature* **543**, 695-699 (2017).
- 572

573 Methods

574 **Synthesis.** $x\text{LTO}-(1-x)\text{LTNO}$ compounds were synthesized by heating the precursors obtained via a sol-
575 gel method, at 650 °C for 10 h in air. To prepare the precursor by sol-gel method, stoichiometric amount of

576 nickel(II) acetate tetrahydrate ($\geq 99.0\%$ (KT), Sigma-Aldrich) and 2% excess lithium acetate dihydrate
577 (reagent grade, Sigma-Aldrich) were first dissolved together in 100 ml of ethanol. Then corresponding
578 amount of titanium(IV) butoxide (97%, Sigma-Aldrich) was slowly added to the solution. After
579 homogeneously mixed, the solution was dried into gel by evaporating ethanol at 80°C under 200 mbar
580 vacuum using a rotary evaporator. The gel was finally dried at 120°C for 8 h.

581 **XRD.** Lab XRD measurements, including *in situ* experiments, were implemented by a BRUKER D8
582 Advance diffractometer with Cu $K\alpha$ radiation ($\lambda_{K\alpha 1} = 1.54056 \text{ \AA}$, $\lambda_{K\alpha 2} = 1.54439 \text{ \AA}$) and a Lynxeye XE
583 detector. XRD and electrochemical data were collected synchronously with a lab-designed air-tight *in situ*
584 cell equipped with a Be window. SXR patterns ($\lambda = 0.458 \text{ \AA}$) were collected via the mail-in service of the
585 11-BM beamline at the Advanced Photon Source at Argonne National Laboratory. To prepare the samples
586 for SXR, the electrode powders were (dis)charged to targeted states followed by their rapid recovery,
587 washing with dimethyl carbonate (DMC) and drying. After that, the powders were sealed in glass capillaries
588 protected by a Kapton sheath. The Rietveld refinements of the SXR patterns were performed by the
589 FullProf program.⁴³

590 **Cell assembly and electrochemistry.** The electrochemistry in liquid cell was performed with 2032-type
591 coin cells, otherwise Swagelok suit was used when specially specified. The cathode powders were made by
592 mixing $x\text{LTO}-(1-x)\text{LTNO}$ compound with carbon (Super P) in a 7:2 weight ratio. The coin cells were
593 assembled in an Ar-filled glovebox, with a Li foil as the anode, two Whatman GF/D borosilicate glass fiber
594 sheets as the separator, and an LP30 electrolyte consisting of 1M LiPF_6 in ethylene carbonate (EC):
595 dimethyl carbonate (DMC) in a 1:1 volume ratio. Galvanostatic charge and discharge method was used to
596 assess the electrochemical performance of $x\text{LTO}-(1-x)\text{LTNO}$ compounds. Short-period GITT tests were
597 carried out stepwise with a 0.5 h pulse at $C/10$ (20 mA g^{-1}) followed by 8 h relaxation, while in long-period
598 GITT the relaxation time was prolonged to 200 h. For CV tests, a three-electrode Swagelok cell was used,
599 with the reference electrode being a piece of lithium attached on a copper wire and sandwiched between
600 two layers of Whatman GF/D borosilicate glass fiber sheets. CV test was performed by scanning the voltage
601 in a rate of 0.05 mV s^{-1} between 1.5 V and 4.8 V versus Li/Li^+ . As for the assembly of ASSB cells, 30 mg
602 of Li_3InCl_6 solid electrolyte was first pelletized by cold pressing at 1 ton/cm^2 for few seconds. Then, 15 mg
603 of $\text{Li}_6\text{PS}_5\text{Cl}$ was evenly dispersed on one side of Li_3InCl_6 pellet and pressed together at 1 ton/cm^2 for a few
604 seconds. After that, a homogeneous powder of $\text{Li}_6\text{PS}_5\text{Cl}:\text{Li}_{0.5}\text{In}$ mixture (40:60 wt.%), as the anode, was
605 spread on the surface of $\text{Li}_6\text{PS}_5\text{Cl}$ pellet. Next, the cathode mixture of 0.4LTO-0.6LTNO, Li_3InCl_6 , and
606 carbon super P (40:80:20 wt.%), mixed by hand grinding for 15 minutes, was pressed on the side of Li_3InCl_6
607 pellet and finally, the whole stack was densified at 4 ton/cm^2 for 15 minutes. After the compression, the
608 ASSB cells were closed with a torque key applying a pressure of 1 ton/cm^2 for electrochemical cycling at
609 room temperature.

610 **Electrochemical titration.** To do the electrochemical titration, about 100 mg of a mixture of Li-Ni-Ti-O
611 with carbon Super P in a 7:2 weight ratio was firstly charged to certain states (e.g. 1st charge 4.8V, 4.5V,
612 and 200 mA h g^{-1}) by using a big home-designed Swagelok-type cell. The powder was immediately
613 extracted from the cell once the charging was finished, and washed with DMC for at least three times. After
614 that, the powder was dried under vacuum ($<1 \text{ mbar}$) for at least 2 hours. The powder was divided into
615 several equal portions, relaxed under different conditions (e.g. fixed temperature but variable dwelling time,
616 or fixed dwelling time but variable temperatures) and sealed in vials under Ar before heating. The heating
617 was performed with a Büchi B-585 glass oven under continuous evacuation or an oven (properly sealed
618 with Al pouches). The relaxed powders were then put back into Swagelok cells with fresh electrolyte and
619 new Li anode to check their discharge behavior.

620 **TEM.** TEM samples were prepared by crushing the crystals in DMC and depositing a drop of suspension
621 onto a carbon film supported by a copper grid. Samples were stored and prepared in an Ar-filled glovebox.
622 A Gatan vacuum transfer holder was used for sample transportation to the TEM column avoiding contact
623 with air. Electron diffraction (ED) patterns, high angle annular dark field scanning transmission electron

624 microscopy (HAADF-STEM) images, and electron energy loss (EELS) spectra were acquired on a probe
625 aberration-corrected Titan Themis Z electron microscope at 200 kV equipped with a Gatan Quantum ER965
626 spectrometer. The EELS spectra were collected using a monochromatic e-beam with energy resolution of
627 0.17 eV measured from the full width at half maximum of the zero-loss peak.

628 **OEMS.** Freestanding electrodes comprised 70% wt. active materials, 20% wt. carbon (Super P) and 10%
629 PTFE were used. An in-house designed OEMS cell was used to run the experiment.⁴⁴ 150 μ L of LP30
630 electrolyte, Li foil as anode and 1 piece of GF/D glassfiber separator were used to construct the half cell.
631 The quantitative gas evolution data on m/z channels of 32 (O_2) and 44 (CO_2) was were collected *operando*
632 with a protocol of resting the cell for 4 h before and 12 h after the full electrochemistry to stabilize the
633 background signal. The OEMS cells were cycled between 1.5-4.8 V for two cycles under C/10 rate. At least
634 two cells were tested for each composition of x LTO-(1- x)LTNO ($x = 0.2, 0.4, 0.5$).

635 **XAS.** Ni, Ti $L_{II, III}$ -edge and O K -edge X-ray absorption spectroscopy (XAS) measurements were carried
636 out at beamline 4-ID-C at Advanced Photon Source (APS) at Argonne National Laboratory (ANL). To
637 verify the electronic environment on the oxide surface, the Ni L -edge spectra were collected in total electron
638 yield (TEY), total fluorescence yield (TFY) and inverse partial fluorescence yield (iPFY) modes. Ti L -edge
639 and O K -edge spectra were collected in TEY and TFY modes at room temperature and under ultra-high
640 vacuum conditions (below 10^{-8} Torr). For iPFY inversion of the non-resonant excited oxygen K -edge
641 fluorescence was used. Contributions from visible light were carefully minimized before the acquisition,
642 and all spectra were normalized by the current from freshly evaporated gold on a fine grid positioned
643 upstream of the main chamber. The measured spectra were aligned using beamline reference and a basic
644 normalization using a linear background. Ni and Ti K -edge XAS experiments were performed at the
645 beamline 9-BM at the Advanced Photon Source, Argonne National Laboratory (ANL). XAS spectra were
646 collected in both transmission and fluorescence mode using ion chamber and vortex detector, respectively.
647 The incident beam was monochromatized by a Si(111) fixed-exit double-crystal monochromator. A Ni
648 metal reference foil was measured simultaneously with each sample for energy calibration. Data analysis
649 was completed using the IFEFFIT package.⁴⁵

650 **HAXPES.** The *ex situ* HAXPES data were collected at GALAXIES beamline of the SOLEIL synchrotron.⁴⁶
651 To prepare the samples with different relaxation states for HAXPES, 50 mg of cathode powder was first
652 charged to 4.5 V and 200 mA $h\ g^{-1}$ (~ 4.4 V) followed by quick recovering from the cell. After washing and
653 drying, the powder was divided into several equal portions for heat treatment at 120°C for different duration.
654 All the heating steps were done in the Ar-filled glovebox. A vacuum chamber was used to transfer the
655 samples from the glovebox to the HAXPES introduction chamber in order to avoid contacting with air. A
656 third-order reflection of a Si (111) double-crystal monochromator was applied to achieve the photon
657 excitation energy of 10 keV. The photoelectrons were collected and analyzed by a SCIENTA EW4000
658 spectrometer, with an energy resolution of 0.22 eV at 10.0 keV for the Au Fermi edge. The analysis chamber
659 pressure was kept at around 10^{-8} mbar during the whole experiment, and no charge neutralizer was required.

660 **DFT+ U calculations.** The Vienna Ab initio Simulation Package (VASP) was used to perform all
661 calculations, within the generalized gradient approximation and the Perdew-Burke-Ernzerhof potential for
662 electron exchange and correlation energy⁴⁷⁻⁴⁹. A 600 eV cutoff energy and $3\times 2\times 6$ k-point mesh were applied
663 to optimize the ground structure within a spin-polarized DFT+ U framework, where the $U_{\text{eff}}=U-J$ was set to
664 6.4 eV for Ni in order to correct the self-interaction error for correlated d electrons⁵⁰. A unit cell of
665 $Li_{14}Ti_7Ni_3O_{24}$ ($= Li_{1.167}Ti_{0.583}Ni_{0.25}O_2$) was used for searching the ground-state structure and subsequent
666 calculations. The searching of ground-state structure was done by minimizing the adjacent transition metal
667 interactions (Supplementary Fig.10a). Li removal was iteratively done by checking the energies of all the
668 possible configurations for every Li composition, as shown in the convex hull (Supplementary Fig.10b).
669 The convergence conditions for all the calculations were set as 10^{-5} eV for electronic loops and $0.02\ eV\ \text{\AA}^{-1}$
670 ¹ for ionic loops.

671

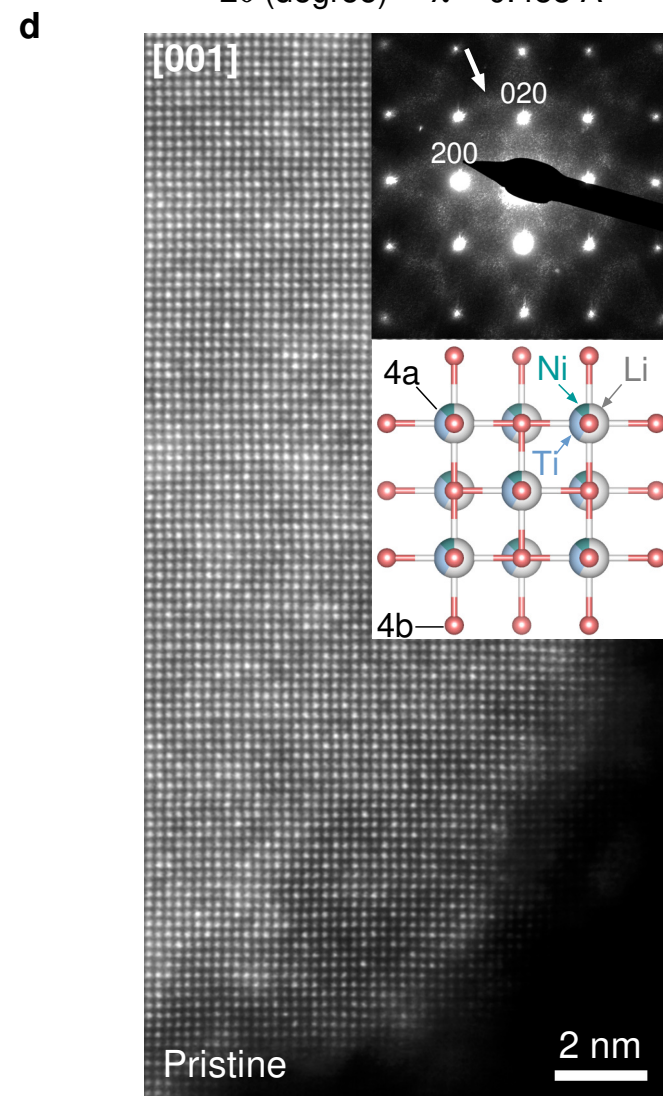
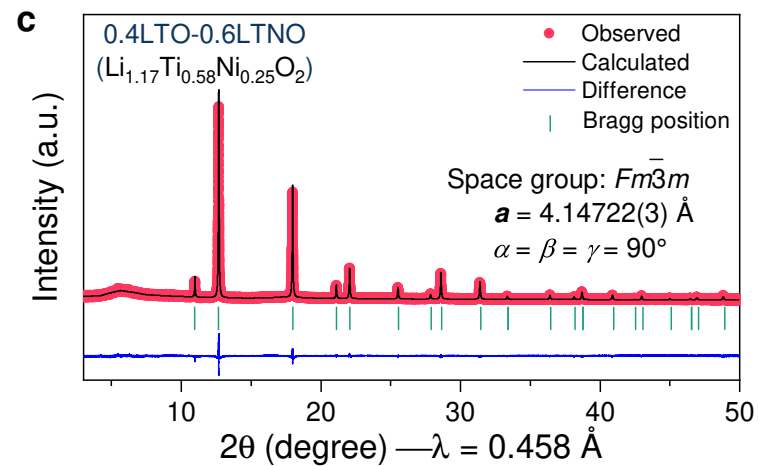
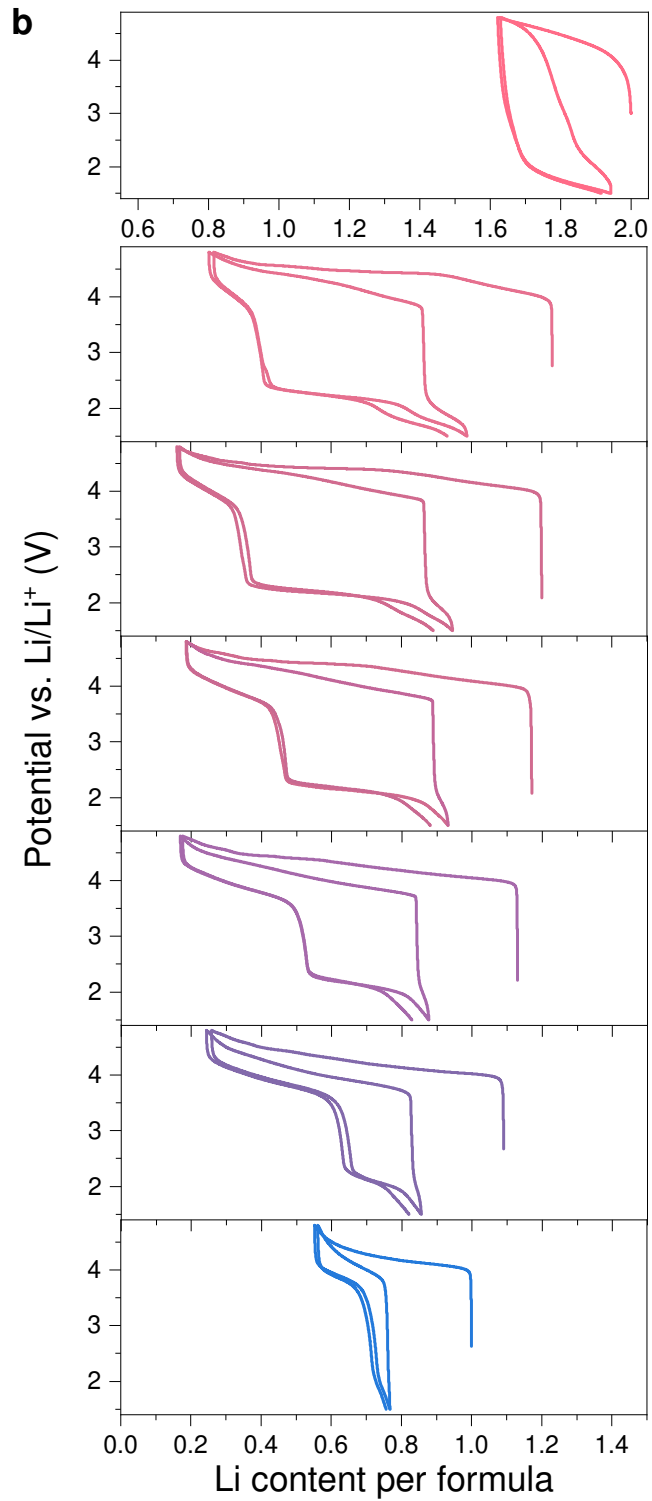
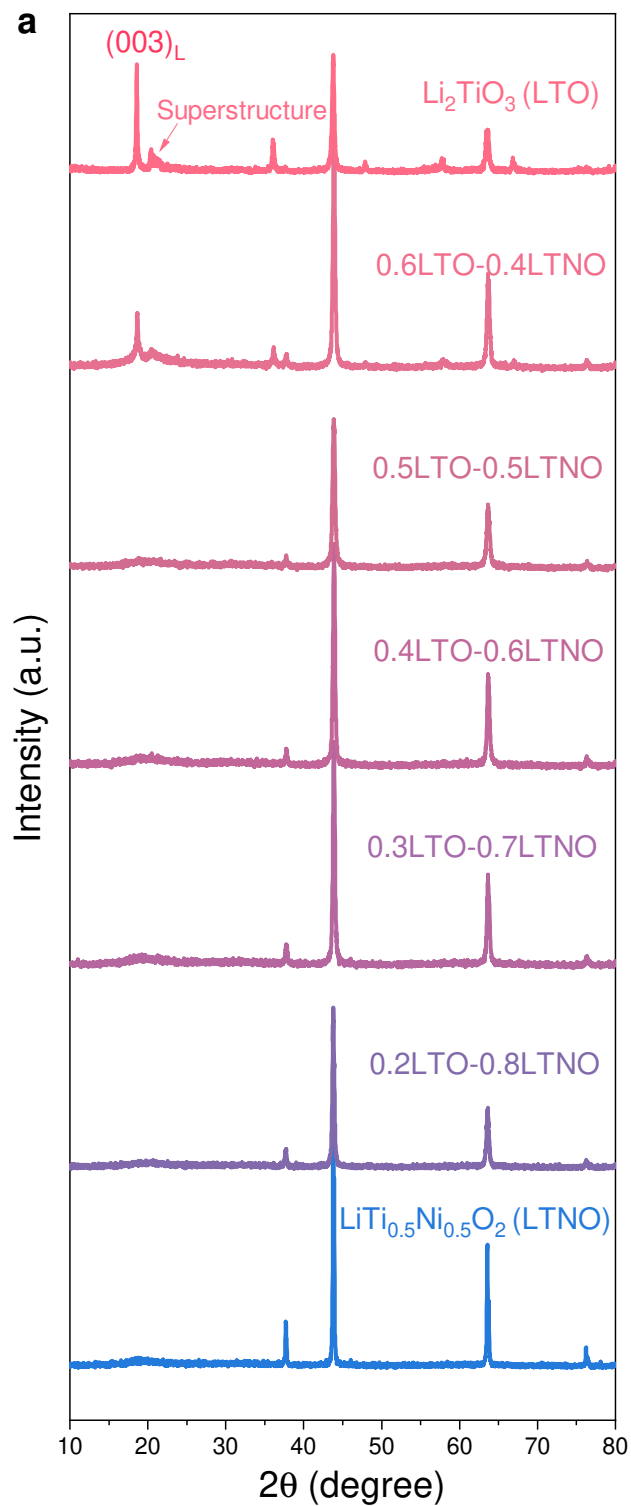
672 **Data availability**

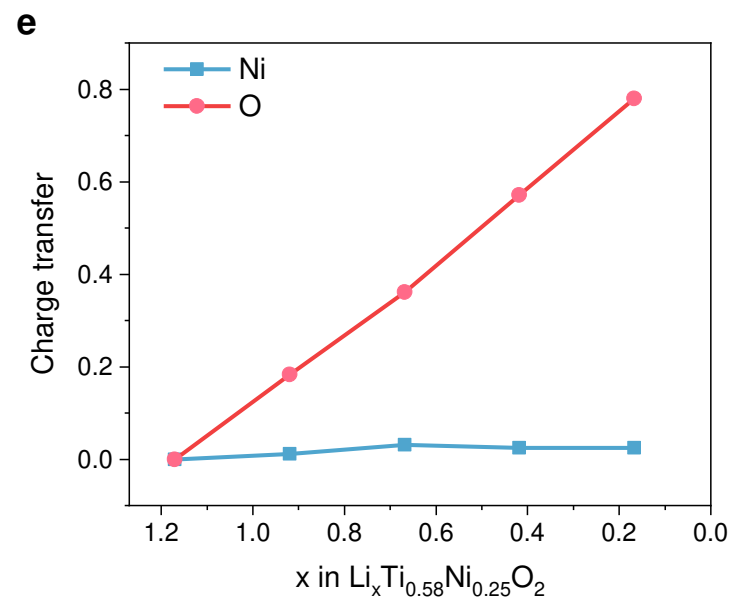
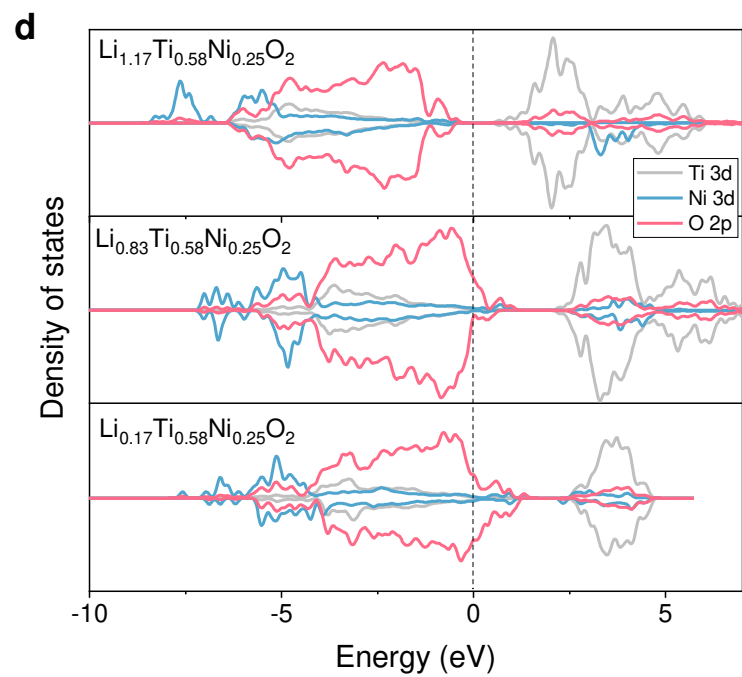
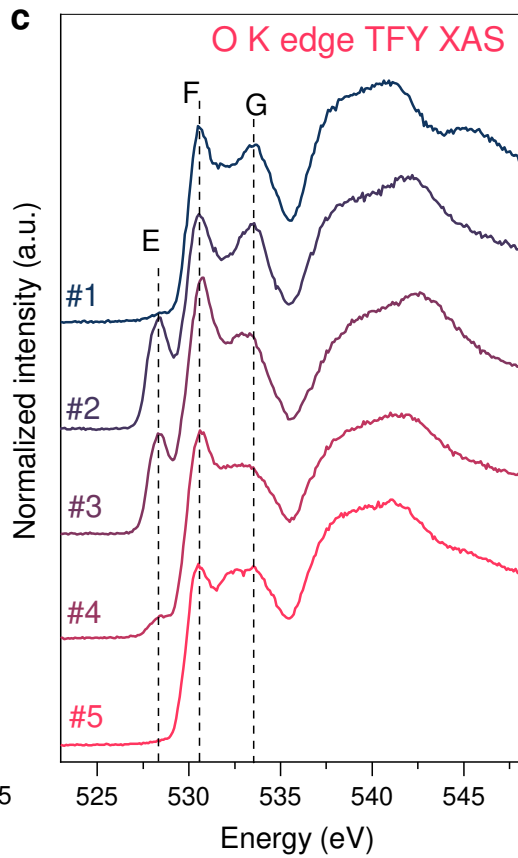
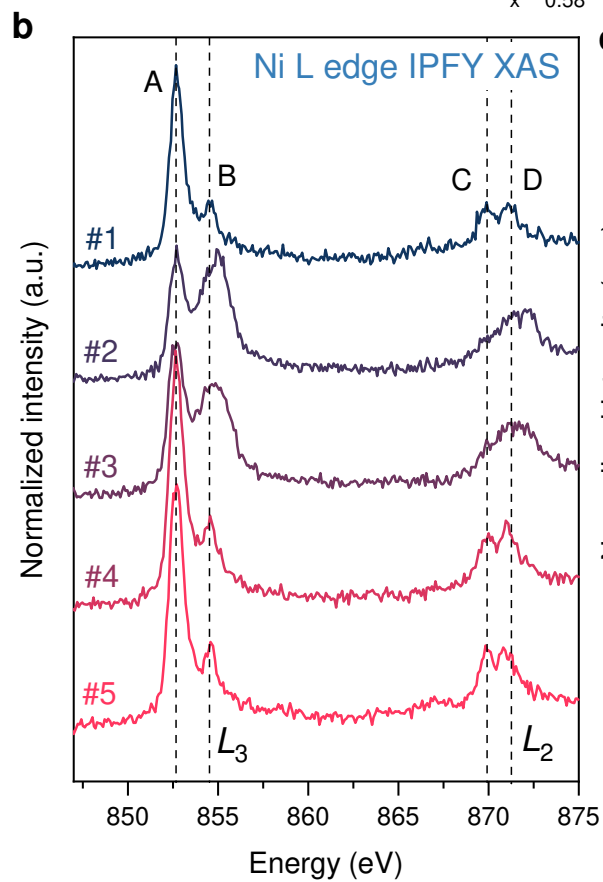
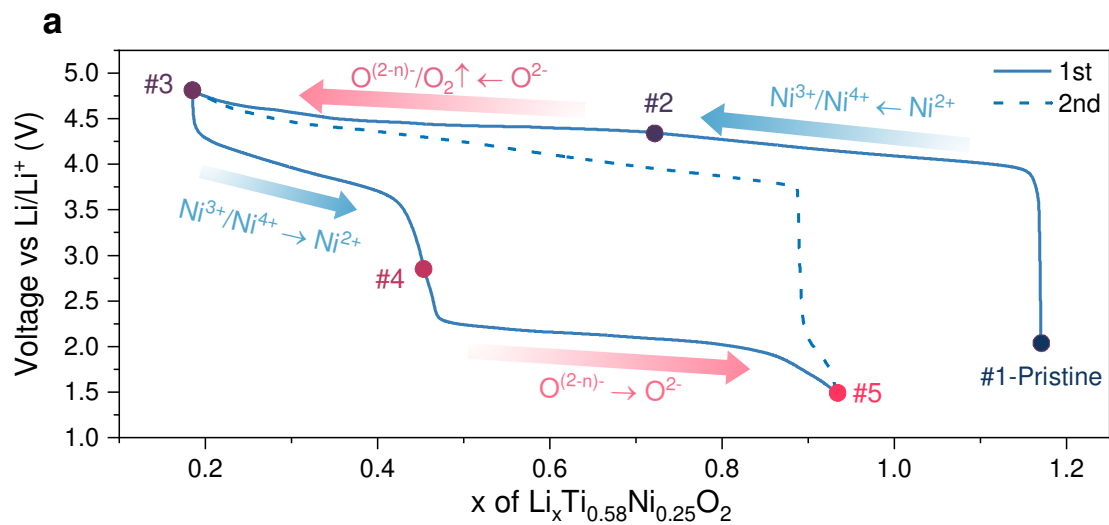
673 All data in supporting the findings of article and its Supplementary Information will be made available upon
674 reasonable request to the authors. Source data are provided with this paper for Fig.1b, Fig.2a, Fig.2d, Fig.2e,
675 Fig.4, and Fig.6a-e.

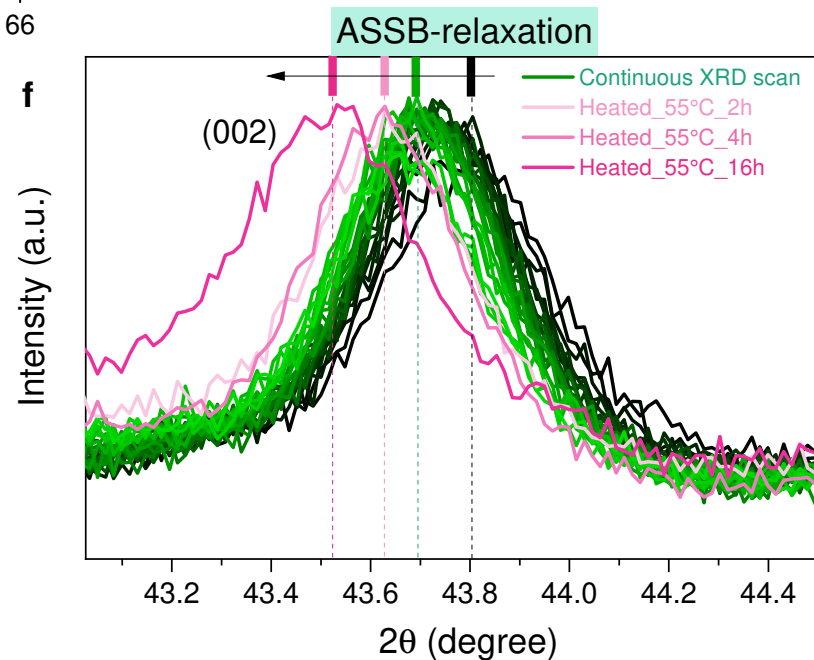
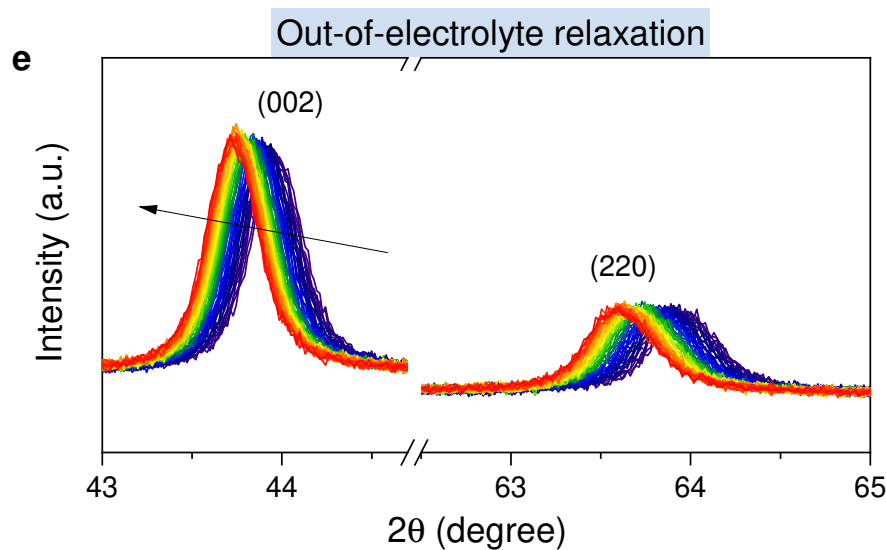
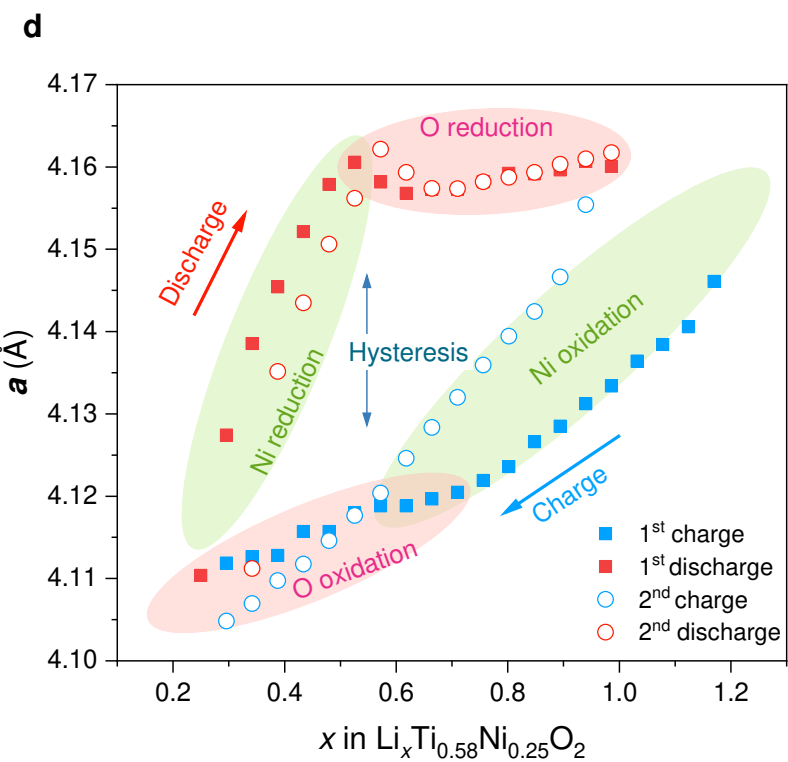
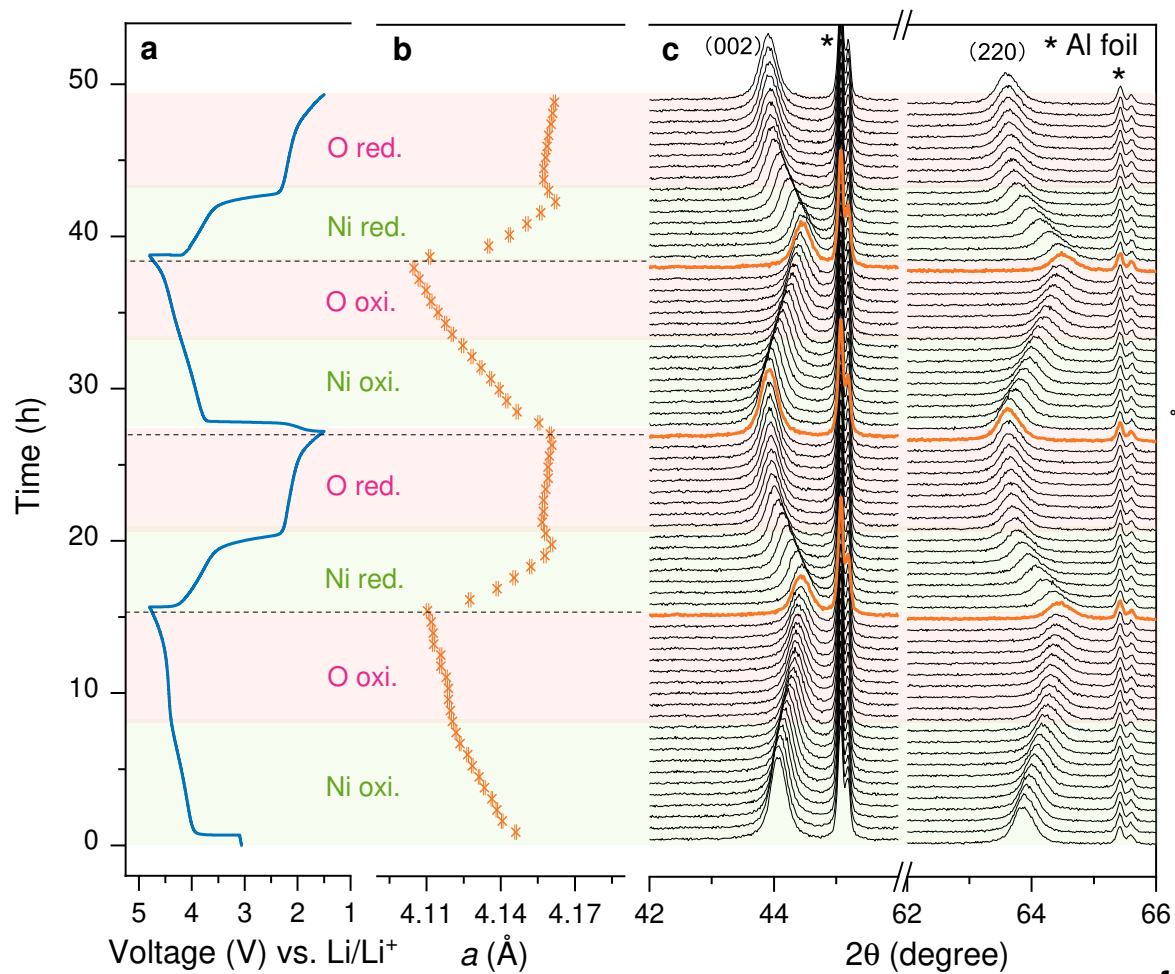
676

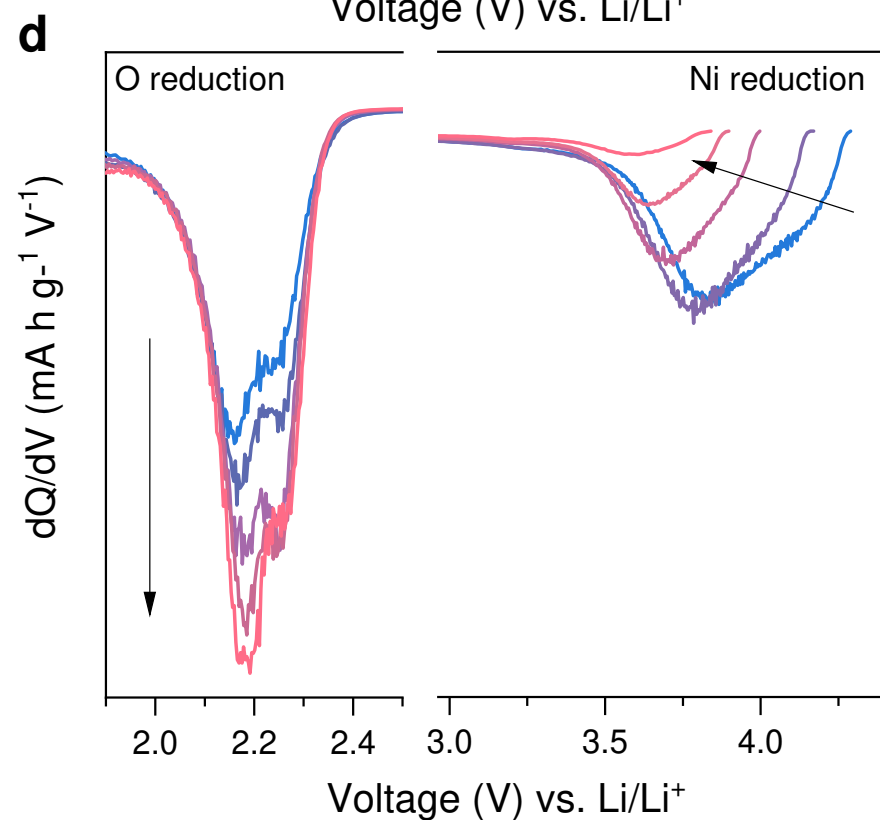
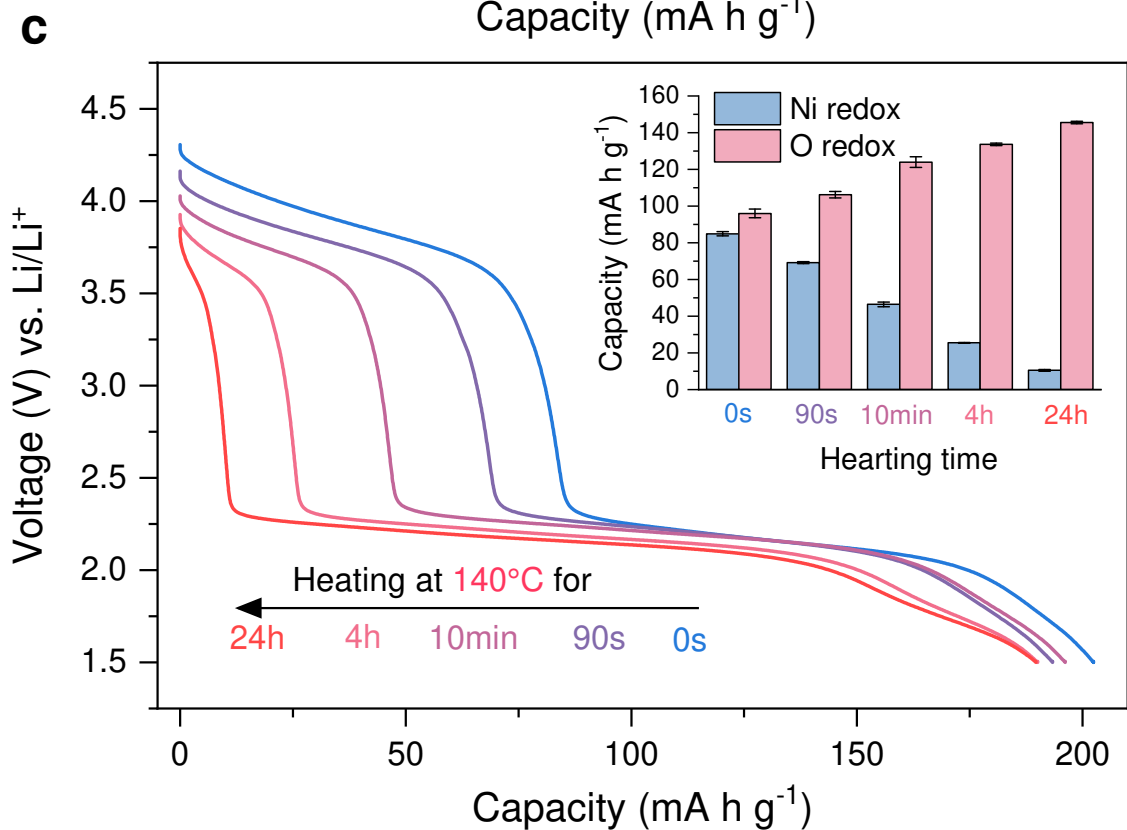
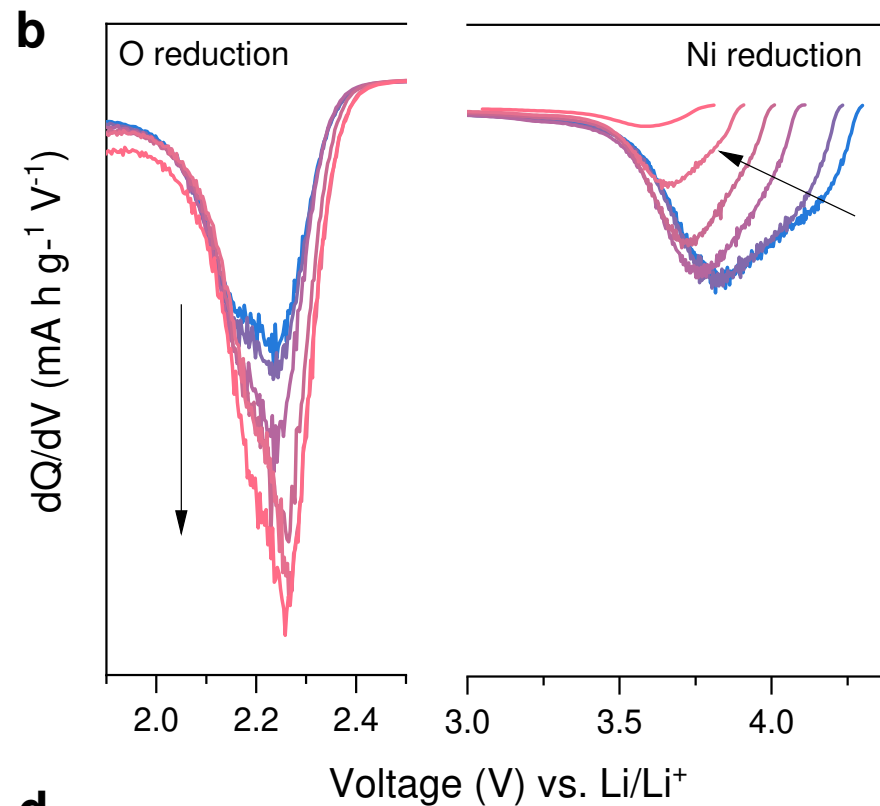
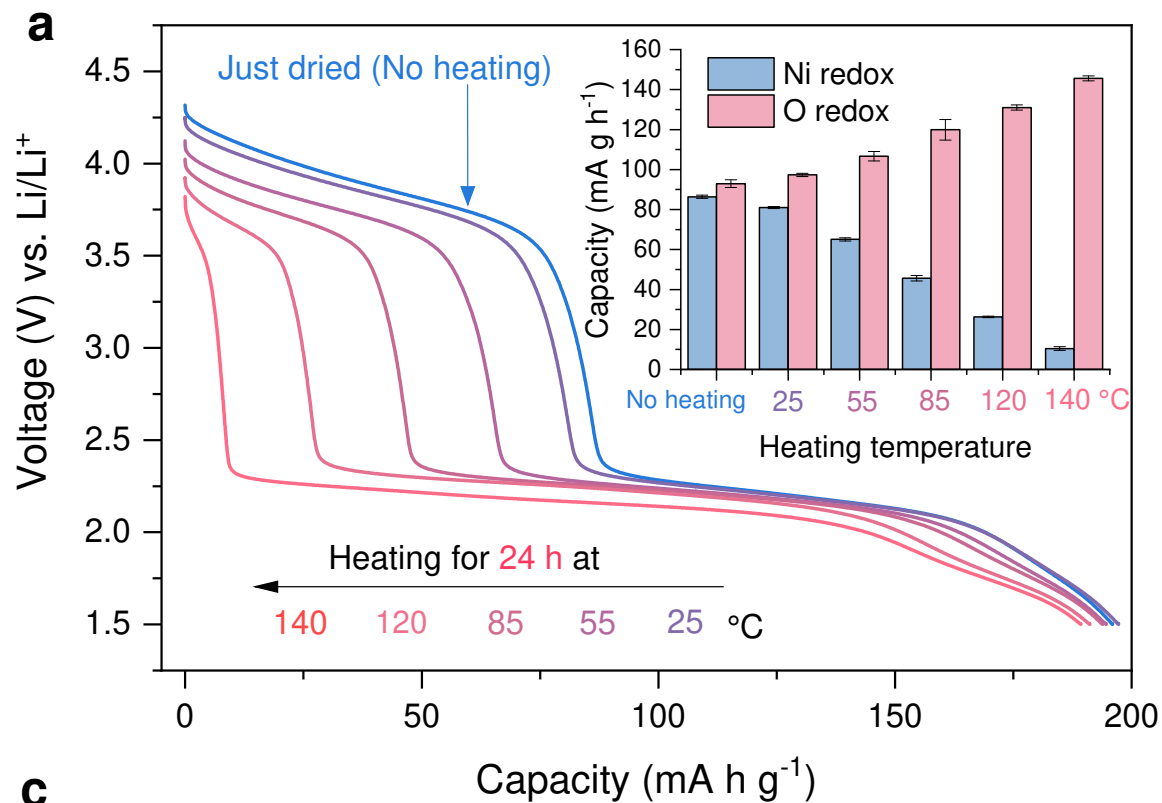
- 677 43. Rodríguez-Carvajal, J. Recent advances in magnetic structure determination by neutron powder
678 diffraction. *Physica B: Condens. Matter.* **192**, 55-69 (1993).
- 679 44. Zhang, L. et al. Unraveling gas evolution in sodium batteries by online electrochemical mass
680 spectrometry. *Energy Storage Mater.* **42**, 12-21 (2021).
- 681 45. Ravel, B. & Newville, M. ATHENA, ARTEMIS, HEPHAESTUS: data analysis for X-ray
682 absorption spectroscopy using IFEFFIT. *J. Synchrotron Radiat.* **12**, 537-541 (2005).
- 683 46. Rueff, J.P., Rault, J.E., Ablett, J.M., Utsumi, Y. & Céolin, D. HAXPES for Materials Science at
684 the GALAXIES Beamline. *Synchrotron Radiat. News* **31**, 4-9 (2018).
- 685 47. Perdew, J.P., Burke, K. & Ernzerhof, M. Generalized Gradient Approximation Made Simple. *Phys.*
686 *Rev. Lett.* **77**, 3865-3868 (1996).
- 687 48. Kresse, G. & Joubert, D. From ultrasoft pseudopotentials to the projector augmented-wave method.
688 *Phys. Rev. B* **59**, 1758-1775 (1999).
- 689 49. Kresse, G. & Furthmüller, J. Efficient iterative schemes for ab initio total-energy calculations using
690 a plane-wave basis set. *Phys. Rev. B* **54**, 11169-11186 (1996).
- 691 50. Wang, L., Maxisch, T. & Ceder, G. Oxidation energies of transition metal oxides within the
692 GGA+U framework. *Phys. Rev. B* **73** (2006).

693

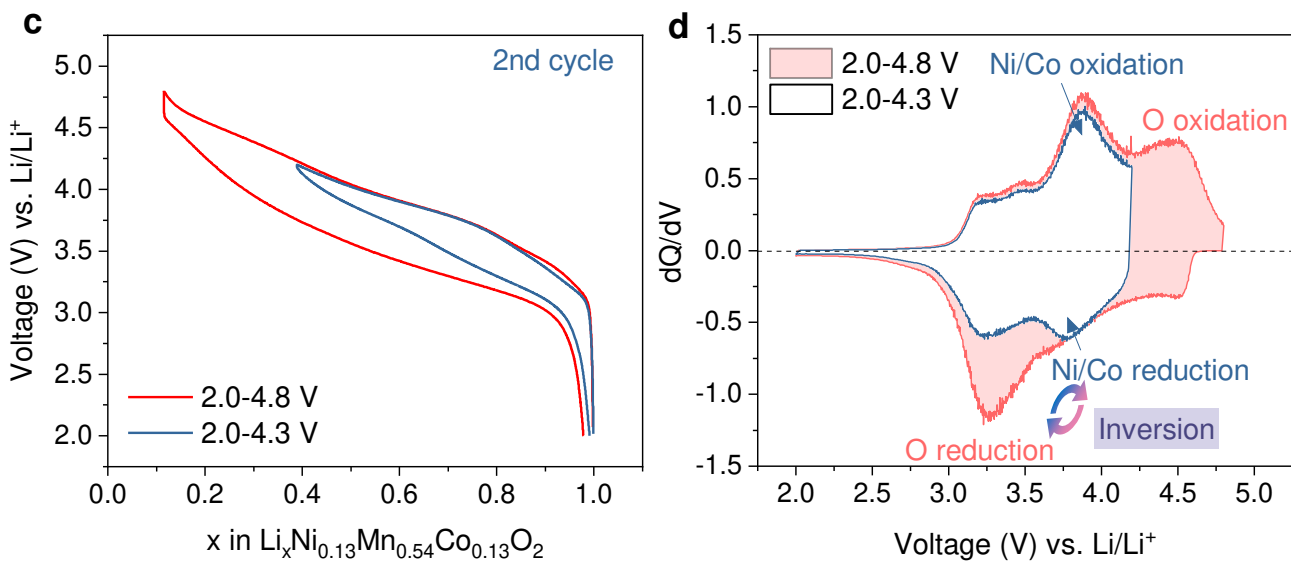
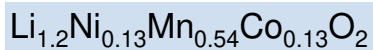
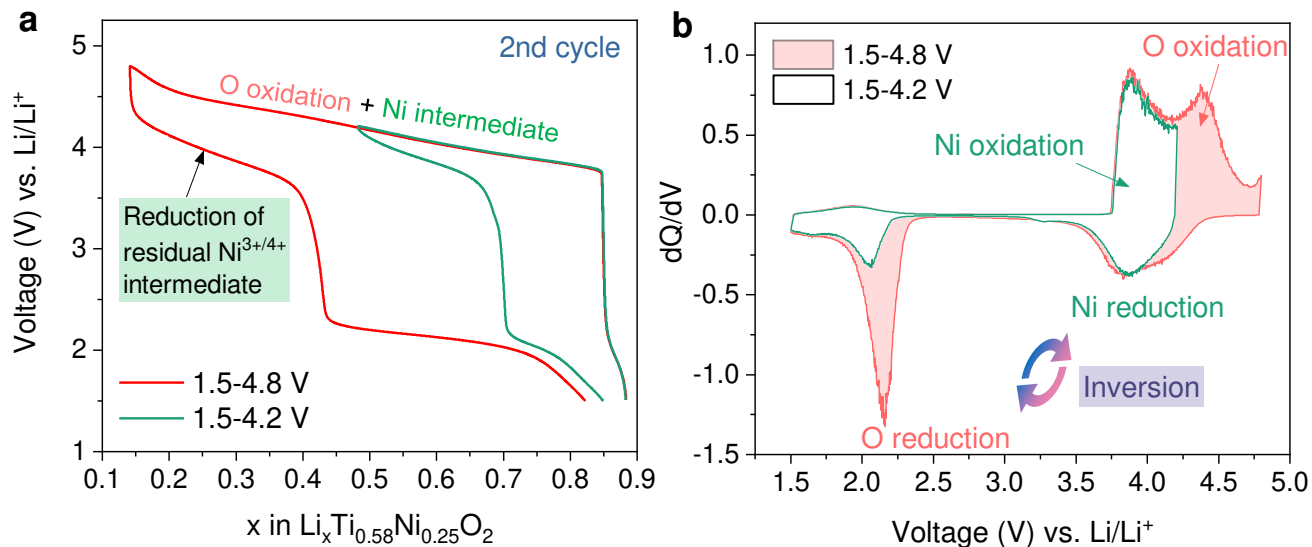
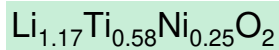








Catioinc-anionic redox inversion



Quantitative picture of voltage hysteresis

